Final Technical Report

Project Title:	Using Solid Particles as Heat Transfer Fluid for use in Concentrating Solar Power (CSP) Plants
Project Period:	02/14/13 – 02/13/16
Reporting Period:	02/14/13 – 02/13/16
Reporting Frequency:	Annual
Submission Date:	03/31/16
Recipient:	The Regents of the University of Colorado
Recipient DUNS #:	007431505
Address:	3100 Marine St Room 475, 572 UCB Boulder, CO 80303-1058
Website (if available)	
Award Number:	DE-EE0005954
Awarding Agency:	DOE EERE SETP CSP subprogram
Working Partners:	Dr. Zhiwen Ma (NREL) Dr. Sreekanth Pannala (SABIC) Dr. Tom O'Brien (consultant – retired NETL)
Cost-Sharing Partners:	
Principal Investigator:	Christine Hrenya Professor Phone: 303-492-7689 Fax: 303-492-4341 Email: hrenya@colorado.edu
Submitted by: **(if other than PI)**	Aaron Lattanzi Graduate Student Phone: 303-492-1356 Fax: 303-492-4341 Email: aala7556@colorado.edu
DOE Contracting Officer:	Lalida Crawford
DOE Technical Contacts:	Levi Irwin and Thomas Rueckert
DOE Project Manager:	Elaine Ulrich

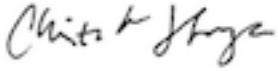

29 March 2016

Signature **Date**

Executive Summary

In today's industrial economy, energy consumption has never been higher. Over the last 15 years the US alone has consumed an average of nearly 100 quadrillion BTUs per year [21]. A need for clean and renewable energy sources has become quite apparent. The SunShot Initiative is an ambitious effort taken on by the United States Department of Energy that targets the development of solar energy that is cost-competitive with other methods for generating electricity. Specifically, this work is concerned with the development of concentrating solar power plants (CSPs) with granular media as the heat transfer fluid (HTF) from the solar receiver. Unfortunately, the prediction of heat transfer in multiphase flows is not well understood. For this reason, our aim is to fundamentally advance the understanding of multiphase heat transfer, particularly in gas-solid flows, while providing quantitative input for the design of a near black body receiver (NBB) that uses solid grains (like sand) as the HTF.

Over the course of this three-year project, a wide variety of contributions have been made to advance the state-of-the art description for non-radiative heat transfer in dense, gas-solid systems. Comparisons between a state-of-the-art continuum heat transfer model and discrete element method (DEM) simulations have been drawn. The results of these comparisons brought to light the limitations of the continuum model due to inherent assumptions in its derivation. A new continuum model was then developed for heat transfer at a solid boundary by rigorously accounting for the most dominant non-radiative heat transfer mechanism (particle-fluid-wall conduction). The new model is shown to be in excellent agreement with DEM data and captures the dependence of heat transfer on particle size, a dependency that previous continuum models were not capable of. DEM and the new continuum model were then employed to model heat transfer in a variety of receiver geometries. The results provided crucial feedback on the efficiency and feasibility of various designs. Namely, a prototype design consisting of an array of heated hexagonal tubes was later supplanted by a vertical conduit with internal baffles. Due to low solids heat transfer on the bottom faces of the hexagonal tubes in the prototype, the predicted wall temperature gradients exceeded the design limitations. By contrast, the vertical conduit can be constructed to continually force particle-wall contacts, and thus, result in more desirable solids heat transfer and wall temperature gradients. Finally, a new heat flux boundary condition was developed for DEM simulations to assess the aforementioned wall temperature gradients. The new boundary condition advances current state-of-the-art techniques by allowing the heat fluxes to each phase to vary with space and time while the total flux remains constant. Simulations with the new boundary condition show that the total boundary heat flux is in good agreement with the imposed total boundary heat flux.

While the methods we have utilized here are primarily numerical and fundamental by nature, they offer some key advantages of: (i) being robust and valid over a large range of conditions, (ii) able to quickly explore large parameter spaces, and (iii) aid in the construction of experiments. We have ultimately leveraged our computational capabilities to provide feedback on the design of a CSP which possesses great potential to become a cost effective source of clean and renewable electricity. Overall, ensuring that future energy demands are met in a responsible and efficient manner has far reaching impacts that span both ecologic and economic concerns.

Regarding logistics, the project was successfully re-negotiated after the go/no-decisions of Years 1 and 2. All milestones were successfully completed.

Table of Contents

Background

As part of the ultimate goal of developing a commercially-viable, transformative method for storage of heat for use in the next generation of concentrating solar power (CSP) plants, the objective of this work has been to develop and validate a first-principles continuum model that describes the flow of solids and heat transfer found in the solid particle receiver. The follow-on intention of the resulting tool is to use it for the design a near-blackbody receiver to meet the SunShot Initiative goals of 6¢/kWh, though this was not included in the scope of the current project being reported on.

This BRIDGE project originally supported the development of a low-cost solid-particle prototype receiver designed by NREL and shown in Figure 1. Such a near-blackbody (NBB) can operate at high temperature, heating stable particles to more than 1000°C. The tube openings receive solar flux directly on their interior surface and transfer the heat to the solid particles flowing down over the exterior of the absorber tube surface. Based on lessons learned from experiments (via SunShot award led by NREL) and simulations (via this BRIDGE award) alike, a second-generation receiver was conceived by NREL and investigated via simulations through this BRIDGE project. The results from both simulation efforts are detailed further below; a more general introduction to the important physics is contained directly below this paragraph.

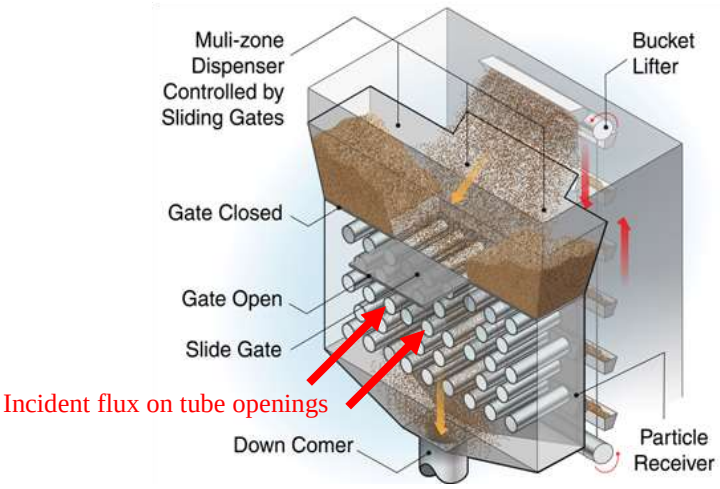

Figure 1. Schematic of NREL prototype receiver using solid particles as the heat transfer fluid.

When considering multiphase heat transfer, two numerical frameworks are of significant importance. The first is the Discrete Element Method (DEM), where the solids phase is treated as discrete-particles. In the absence of radiation, the relevant heat transfer mechanisms for DEM are as follows: particle-particle (PP) conduction, particle-fluid-particle (PFP) conduction, particle-wall (PW) conduction, particle-fluid-wall (PFW) conduction, and interphase convection. The conduction mechanisms may be grouped into direct mechanisms (PP, PW), acting through solid body contact, and indirect mechanisms (PFP, PFW), acting through a thin layer of interstitial fluid. Only the indirect and direct conduction mechanisms pertaining to heat transfer with a wall will be expounded upon here, since our initial DEM simulations revealed these to be the dominant mechanisms. The second numerical framework is the Two Fluid Model (TFM), which, in contrast

to DEM, treats the solids phase as a continuum. Since TFM no longer resolves individual particles, attempts to close the solids heat flux have primarily been through the development of effective thermal conductivities, which aim to account for all of the aforementioned mechanisms in DEM. The predominant closure for the effective thermal conductivity will be described in detail below.

DEM Direct Conduction Mechanism (Particle-Wall)

Direct conduction occurs across the mutual contact area between two bodies and is shown schematically in Figure 2. Typically this mechanism is assumed to have little contribution to the overall heat transfer because (i) the contact area between colliding bodies is small and (ii) collisions are brief **[**6**]**. In denser flows with enduring contacts (as is expected as particles flow over the heat exchanger tubes), however, contact conduction may be significant. The contact conduction model implemented in MFIX, the open-source software that serves as the basis for this project, is an extension of the model developed by Batchelor and O'Brien [7]. That model assumes the two colliding particles have equivalent diameters and thermal conductivities, but these assumptions have been relaxed in the current version of MFIX. The Batchelor and O'Brien method computes the contact area from Hertzian theory and depends on material properties. MFIX, however, has multiple contact models (i.e., Hertzian and linear spring dashpot) and thus the Batchelor and O'Brien method has been modified within MFIX to allow for different contact laws. Namely, instead of the contact area being computed from Hertzian theory, the contact area is alternatively computed from the geometric configuration of the two colliding bodies. Closure for the heat transferred across the contact area between a particle and wall is:

$$\dot{Q}_{pw} = h_{pw}\left(T_w - T_p\right) = 4\frac{k_p k_w}{k_p + k_w}\left(T_w - T_p\right) = 4k_{eff}R_C\left(T_w - T_p\right) \qquad (1)$$

where κ_{eff} is an effective solids conductivity and R_c is the contact radius.

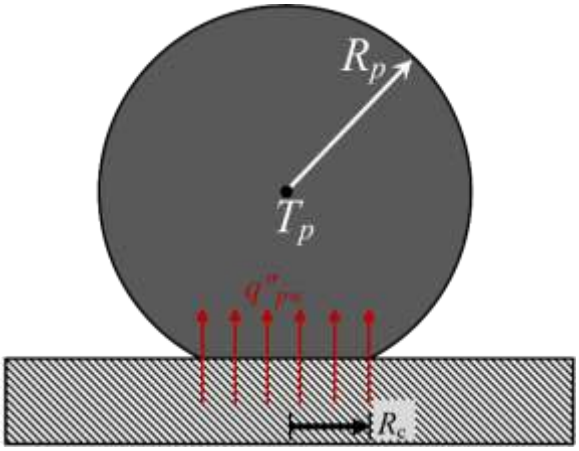

Figure 2. A schematic showing the heat transfer across the mutual contact area between a particle and a wall.

DEM Indirect Conduction Mechanism (Particle-Fluid-Wall)

Indirect conduction can be viewed as an enhancement to contact conduction and is found in our simulations to be a dominant heat transfer mechanism. Heat can be transferred across the stagnant fluid within the small interstitial gaps that occur when two surfaces (particle or wall) are

close to one another or touching. The Rong and Horio model [8], shown schematically in Figure 3 for a particle-wall configuration, predicts this particle-fluid-wall conduction and has been implemented in MFIX. Each particle is assumed to be surrounded by a lens of stagnant fluid. The stagnant, gas-layer thickness (δ_{lens}) is a specified parameter and the recommended value is $1/5^{th}$ of the particle radius, as suggested in [9]. The heat transfer is assumed to be in one direction, along the axis connecting particle centers or in the wall normal direction for particle-wall contacts. Accordingly, the total heat transferred through the interstitial fluid in the Rong and Horio model (Eq. 2) is obtained by integration in regions where the bodies are not in direct contact but instead where the fluid lenses overlap. For particle-wall contacts, the integration is done in regions where the particle lens overlaps the wall. This heat transfer is an enhancement to contact conduction because the effective thermal contact area between particles is significantly increased.

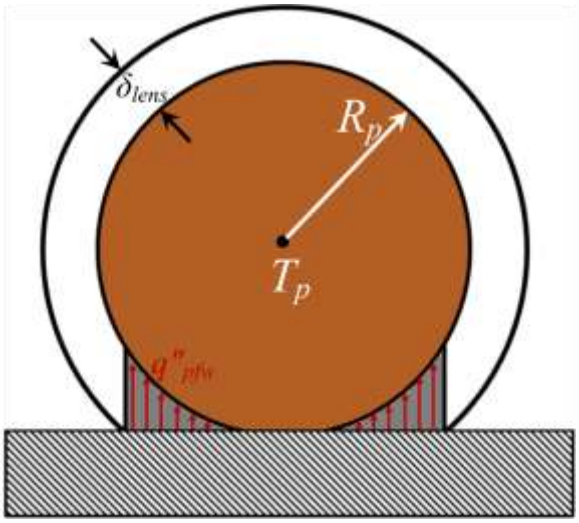

Figure 3. A schematic showing heat transfer via conduction through the stagnant interstitial fluid between a particle and a wall.

The particle-fluid-wall heat transfer predicted by the Rong and Horio model is:

$$\dot{Q}_{pfw} = h_{pfw}(T_w - T_p) = \int_{r_{min}}^{r_{max}} \frac{2\pi K_g r}{Max(l,s)}(T_w - T_p)dr \qquad (2)$$

where κ_g is the gas thermal conductivity, l is the gap distance between the wall and the surface of the particle, s is the minimum gap distance, and r_{min} and r_{max} are geometric variables that depend on the particle overlap and lens radius. The above integral becomes singular as the gap distance approaches zero (where the particle contacts the surface). To avoid this singularity, a minimum threshold gap distance is utilized (s). The two input parameters for the Rong and Horio model are the lens thickness, δ_{lens}, and the assumed minimum gap distance, s. A scaled lens thickness (δ/R_p) of 0.40 was employed here, while the minimum gap distance was set equal to the mean free path of the gas (2.75×10^{-8} m). The mean free path is chosen since rarefaction effects reduce the gas thermal conductivity for gap distances less than the mean free path.

TFM Thermal Conductivity

Within TFM, the conductive heat flux (q_s'') for the solids phase is modeled using Fourier's law:

$$q_s'' = -\varepsilon_s \kappa_s \nabla T_s \tag{3}$$

where the solids volume fraction is ε_s and T_s is the thermal temperature of the solids phase. The solids phase thermal conductivity, κ_s, is closed by using a model based on work by Kuipers, Prins, and van Swaaij **[**17, 18**]**. The solids conductivity consists of contributions from terms including the solids conductivity as well as the fluid phase conductivity **[**19**]**. This model accounts for conduction through the mutual contact area between particles as well as indirect conduction through the wedge of stagnant interstitial gas trapped between the particles but the contributions from radiative heat transfer are neglected. The solids phase thermal conductivity is:

$$\frac{\kappa_s}{\kappa_g} = \frac{\left[\phi A + (1-\phi)\Gamma\right]}{\sqrt{1-\varepsilon_g}} \tag{4}$$

$$\Gamma = \frac{2}{\left(1-\frac{B}{A}\right)}\left[\frac{(A-1)}{\left(1-\frac{B}{A}\right)^2}\frac{B}{A}\ln\left(\frac{A}{B}\right) - \frac{(B-1)}{\left(1-\frac{B}{A}\right)} - \frac{1}{2}(B+1)\right] \tag{5}$$

$$B = 1.25\left(\frac{1-\varepsilon_g}{\varepsilon_g}\right)^{10/9} \tag{6}$$

$$A = \frac{\kappa_p}{\kappa_g} \tag{7}$$

The parameter ϕ in Eq. 4 is the estimated fractional contact area and the recommended value of 7.26×10^{-3} is used in MFIX and the expression for B in Eq. 6 is for spherical particles. The above constitutive relation for the solids phase thermal conductivity is derived for packed beds, however, it is often used for more dilute systems such as the fluidized bed heat exchanger **[**18**]**.

Project Objectives

This project supported the SunShot goal of 6¢/kWh for concentrating solar power (CSP) by 2020, via a "bridge" of this BRIDGE award to the NREL Sun Shot award (PI: Zhiwen Ma). This BRIDGE award focus was on the development of a first-principles model that can ultimately be used for design and optimization of a solar receiver using solid grains as a heat transfer fluid. The three-year project was successfully re-negotiated after Years 1 and 2. The complete set of tasks and milestones for the 3-year project are given below, which is taken directly from the SOPO. To save space, milestone tables are filled in here and will be described in the Project Results and Discussion section below.

YEAR 1

Task 1: Model Verification/Validation for Non-Radiative Heat Transfer

The focus of budget period one (BP1) is to validate the continuum model that predicts the heat transfer to solid particles falling around a single, non-radiating heated cylinder. The continuum model is validated by comparison to DEM simulations. These simulations are also used to better understand the important mechanisms by which energy is transferred to the solid particles and the hydrodynamic behavior in a solar receiver. The specific tasks and milestones in the SOPO for this budget period are shown below.

- Subtask 1.1: Train the new project personnel in modeling techniques (DEM and continuum) and tools (MFIX simulator). Identify recent DEM and experimental data and existing DEM simulations, without radiation effects, and for use in validating continuum model.

- Subtask 1.2: Generate MFIX DEM simulation data of simplified geometry mimicking solar collector (e.g., single horizontal heat transfer tube with solid particles flowing from above) for use in validation of continuum model without radiation. A range of flow parameters (e.g., solids flux) and particle properties (e.g., particle size) will be examined.

- Subtask 1.3: Perform MFIX continuum simulations for datasets associated with Tasks 1.1 and 1.2 to critically assess model validity for case of no radiation. Model verification (numerical accuracy) will be accomplished via mesh-refinement for the single-tube system. Model validity will be accomplished via evaluation of closure models for heat transfer effects (e.g., conduction, convection).

Milestone (Task 1): Demonstration of the validity of the non-radiative continuum model via comparisons with experimental and/or DEM data sets, and specifically a predicted heat transfer coefficient with accuracy of 80-90%.

Task 2: Initial Assessment of MFIX Radiation Model

Here we look ahead to the MFIX radiation model and assess its status in preparation for tasks in next budget period, with particular attention to any new developments / releases since project commencement.

- Subtask 2.1: Identify the radiation mechanisms contained in the most recent release of MFIX for both DEM and continuum model, and contact other research groups working on radiation models to determine their status and potential release dates.

Milestone (Task 2): Document describing the state of the radiation models in most recent version of MFIX, and listing of radiation mechanisms that need to be incorporated into the software for work in upcoming budget periods. The specific challenges associated with each radiation mechanism will be identified and strategies to address those challenges will be described.

Go/No-Go Decision Point 1
Successful completion of all the milestones in Budget Period 1. Also, for case of non-radiative heat transfer, deliver a favorable comparison (90% accuracy of heat transfer coefficient) between continuum model predictions and experimental data and/or DEM simulations.

YEAR 2

Task 3: Validation of Hydrodynamics and Heat Transfer Model for Hexagonal Array

The focus of budget period two (BP2) is to validate the non-radiative continuum heat transfer model for falling particles flowing through an array of heated hexagonal tubes. Validation will be performed by comparison to 'ideal' DEM data. These simulations will build off of budget period 1 and assess the validity over a range of particle sizes, hexagon apex angle, tube spacing (in the horizontal and vertical directions), and mass flow rate. The simulations will also be used to aid design of the solar receiver by better understanding the fundamental mechanisms by which heat is absorbed by the solid particles and also offering guidance on how to improve the performance.

- Subtask 3.1: Extend continuum model for particle-wall heat transfer to correctly capture particle size effects. Compare new continuum predictions to DEM data for particles at heated wall. These results will be submitted for journal publication.
- Subtask 3.2: Generate DEM validation data for particle flow through a heated hexagonal array. The array configuration will be guided by the experimental system at NREL (~16 hexagonal-tube array).
- Subtask 3.3: Perform continuum simulations for same system in Subtask 3.2. Perform comparison between DEM and continuum predictions, with special emphasis on hydrodynamic instabilities and their effects on heat transfer. These results will be submitted for journal publication.

Milestone (Task 3): Using particle flows in their fully developed state, demonstrate the validity of the continuum model for a hexagonal array via comparisons with DEM data sets. Criterion for validation is a satisfaction of the terms stated in Milestone Task 3 Conclusion Table shown below. Continuum heat transfer coefficients will display on average ≤ 20 percent error when compared to the DEM heat transfer coefficient. The comparison will occur over multiple configurations as described in Milestone Table Task 3 below. The data in Milestone Table (Task 3) will be used to generate a Tukey Mean-Difference Plot. Two papers will be submitted for publication in a peer-reviewed journal. The Nusselt number will be plotted for different horizontal and vertical spacings, different apex angles, different particle sizes, and mass flow rates; all as defined in **Milestone Table (Task 3)**. The Nusselt number is defined as $\mathrm{Nu} \equiv hL/\kappa_g$, where h is the heat transfer coefficient, L is a characteristic length (width of tube), and κ_g is the thermal conductivity of air. The heat transfer coefficient is defined as the total heat transfer rate (conduction + convection) per hexagon surface area divided by the temperature difference between the wall and inlet solids temperatures.

$$\bar{h} = \frac{\dot{Q}_{tot}}{A_{hex,tot}\left(T_{wall} - T_{s,inlet}\right)} \tag{8}$$

Milestone Table (Task 3)

Variable[1]	Heat Transfer Coefficient			
	Continuum [W/m^2-K]	**DEM** [W/m^2-K]	**Percent Error**	**Previous Continuum Model**
Particle Size (100microns)	1098.7	997.23	10.18%	--
Particle Size (200microns)	869.56	780.34	11.43%	*218.78 (72% Err)*
Particle Size (300microns)	494.73	487.41	1.50%	*230.93 (53% Err)*
Vertical Tube Spacing (4.98 cm)	494.73	487.41	1.50%	*230.93 (53% Err)*
Vertical Tube Spacing (5.52 cm)	465.66	465.22	0.10%	*199.92 (57% Err)*
Vertical Tube Spacing (4.50 cm)	447.52	446.01	0.34%	*201.09 (55% Err)*
Horizontal Tube Spacing (5.04 cm)	494.73	487.41	1.50%	*230.93 (53% Err)*
Horizontal Tube Spacing (4.80 cm)	481.17	484.90	0.77%	*238.72 (51% Err)*
Horizontal Tube Spacing (4.44cm)	661.77	584.16	13.29%	*286.90 (51% Err)*
Apex Angle 89°	494.73	487.41	1.50%	*230.93 (53% Err)*
Apex Angle 75° (Hex Height = 8.7 cm)	406.01	371.42	9.31%	*194.23 (48% Err)*
Apex Angle 60° (Hex Height = 10.38 cm)	385.70	344.14	12.08%	*195.26 (43% Err)*
Maximum Mass Flow Rate (258 kg/s-cm^2)	494.73	487.41	1.50%	*230.93 (53% Err)*
0.5 of Mass Flow Rate	320.91	313.28	2.44%	*181.53 (42% Err)*
Please provide the average (as shown) *and* the standard deviation →			$\frac{1}{n} * \sum_{1}^{n} \frac{\lvert x_{i,DEM} - x_{i,Continuum} \rvert}{x_{i,DEM}}$	
			Average = 5.69% (Base case counted once)	

Success in Milestone (Task 3) is defined as the one-sided Student's t-test conclusion at 95% confidence interval that there is no statistically significant difference between the mean error of all modeled Continuum and DEM Heat Transfer Coefficients and error values less than or equal to the target of 0.20, expressed as:

$$\left[T_{one\ sided,95\%\ CI}\right]; \quad \frac{1}{n} * \sum_{1}^{n} \frac{\lvert x_{i,DEM} - x_{i,Continuum} \rvert}{x_{i,DEM}} \leq 0.20 \qquad (9)$$

Milestone Task 3 Conclusion Table.

$\frac{1}{n}\sum_{1}^{n} \frac{\lvert x_{i,DEM} - x_{i,Continuum} \rvert}{x_{i,DEM}}$	**Success Value**	**Method of Evaluation**	**Required t-value**	**Computed t-value**	**Milestone Met?**
5.67% +/- 5.67% (stdev)	≤0.20	One sided t-test	1.860 (95% and n=9)	7.57 (>99.99% CI)	Y

Task 4: Comparison of DEM and continuum models to laboratory scale

- Subtask 4.1: Identify available experimental data and select one set of flow conditions such as tube size and spacing as well as the particle properties to simulate.
- Subtask 4.2: Perform DEM simulations for the corresponding experimental conditions.
- Subtask 4.3: Perform continuum simulations for the above conditions

Milestone (Task 4): Benchmark the quality of the DEM and continuum simulations by comparing the local heat transfer coefficients to available experimental data. Successful completion of this Milestone will show that the DEM and continuum simulations are able to predict the integrated (or total) heat transfer coefficient with an accuracy greater than 70%. Error bars will be provided for the experimental runs, through either repeat experiments and/or an estimation of the accuracy of the measurement systems and a formal propagation of error analysis.

Task 4B (Contingency plan): If experimental data are not available, the DEM and continuum models can be used to aid design by identifying trends in how the heat transfer coefficient changes for different receiver configurations. Examples of such trends include: hexagonal tube size (width and height), optical properties, particle-tube coefficient of restitution, tube inclination angle, etc. The specific parameter studied will be selected based on input and needs from NREL, but the ultimate goal will be to define the Nusselt number as a function of the parameters in **Milestone Table (Task 3)** and the additional parameter in **Milestone 4.1**. The Nusselt number is defined as $\mathrm{Nu} \equiv hL/\kappa_g$, where h is the heat transfer coefficient, L is a characteristic length (width of tube), and κ_g is the thermal conductivity of air

Go/No-Go Decision Point 2
All tables from this SOPO will be presented in the Phase 2 Continuation Request Report and in the continuation request presentation, including the Tukey Mean-Difference Plots. By the end of Phase 2 we will have used particle flows in their fully developed state to demonstrate the validity of the continuum model for flow through a hexagonal array via comparisons with DEM data sets. Criterion for validation is heat transfer coefficient with accuracy of $\geq 80\%$.

YEAR 3

Task 5: Enhancement of heat transfer for gas-solid flow within a vertical conduit: geometric configuration and mild fluidization

The main focus of Task 5 is placed upon the effects of system geometry and gas fluidization upon the heat transfer, with subsidiary work related to identification of undesirable hot spots along the conduit walls. Simulation conditions will been guided by NREL, so as to parallel the design and experimental apparatus as best as possible. Previous work with a hexagonal tube array design illustrated that to make the NBB receiver viable, the heat flux gradients must be reduced while the particle outlet temperatures are increased. For these reasons, special attention will be paid to promoting more uniform heat transfer coefficients and boosting particle residence time.

- Subtask 5.1: Develop a baseline. Normalization of subsequent work by a control will concisely illustrate the effect of altered parameters on the heat transfer coefficient. Free falling particles through a vertical conduit with constant wall temperatures has been selected as the baseline.

- Subtask 5.2: Introduce baffles into the heated conduit. With an aim at improving heat transfer through interphase mixing, baffles will be staged at various locations throughout the column and their orientation altered.

- Subtask 5.3: Introduce gas momentum point sources (MPSs) (i.e., mild fluidization). To further promote mixing and particle residence time, pulsed and continuous gas injection will be explored.

- Subtask 5.4: Estimate the gradients in wall temperature by either implementing a constant heat flux boundary condition (without radiation) or identify potential hot spots using local heat flux data.

Milestone (Task 5): Criteria for success has been set as the acquisition of a design configuration that yields a time averaged overall heat transfer coefficient (TAOHTC) which meets 80% of the target 400 [W/m^{2}K] for non-radiative mechanisms. The methods for calculating an average heat transfer coefficient (Eq. 10), overall heat transfer coefficient (Eq. 11), and target value comparison (Eq. 12) are outlined below. These metrics will be used to assess the efficiency of multiple configurations, described in Table 1 at the bottom of this section.

$$H_{average} = \frac{\int \frac{q''}{\Delta T} \partial A}{\int \partial A} \tag{10}$$

$$q'' = Total\ Local\ Heat\ Flux \qquad \Delta T = T_{wall} - T_{solids,local}$$

The average heat transfer coefficient is defined as the spatial average of all the local heat transfer coefficients.

$$H_{system} = H_{average,wall} \frac{Area_{wall}}{Area_{total}} + H_{average,baffle} \frac{Area_{baffle}}{Area_{total}} \tag{11}$$

The overall heat transfer coefficient is defined as the area weighted average of the average heat transfer coefficients for the walls and baffles (when applicable).

$$-t_{0.95} \frac{\sigma}{\sqrt{N}} \leq \left(\overline{H_{system}} - 320\right) \tag{12}$$

$$N = Sample\ Size \quad \sigma = Sample\ Variance \quad t_{0.95} = 95\%\ Confidence\ t\ Value \quad \overline{H_{system}} = TAOHTC$$

A left handed Student's t-test with an alpha value of 0.05 will be used to compare the TAOHTC to the target value. Task 1 success occurs if the right hand side of the equation is greater than or equal to the left hand side.

Milestone Table (Task 5)

Variable	H_{system}	% Dev From Baseline	% Dev From *Configuration 3*
Baffle Vertical Spacing 1	147	320	-81
Baffle Vertical Spacing 2	165	371	-78
Baffle Vertical Spacing 3	265	657	-65.5
Baffle Angle 1	601	1617	-22
Baffle Angle 2	743	2022	-3.5
Baffle Angle 3	1130	3128	46.75
Baffle Configuration 1	78	123	-90
Baffle Configuration 2	215	514	-72
Baffle Configuration 3	770	2466	0
Continuous MPS Location 1	447	1177	-42
Continuous MPS Location 2	433	1137	-43
Continuous MPS Location 3	426	1117	-44
Pulsed MPS	445	1171	-42
Calculation of Percent Deviation From Baseline		$= \frac{H_{trial} - H_{baseline}}{H_{baseline}}$	

Task 6: Enhancement of heat transfer for gas-solid flow within a vertical conduit: particle properties (size distribution and roughness) and free convection

While the focus in task 6 is still centered upon the bolstering of heat transfer in a heated vertical conduit, emphasis shifts to more fundamental considerations. The simulation in Task 5 showing the best heat transfer characteristics will be used as the new baseline in Task 6. With this set geometry, the effects of particle size distribution (PSD) and surface roughness on the heat transfer coefficient will be explored. In addition, an order-of-magnitude approximation of the buoyancy forces generated from free convective gas flow within the conduit will be made. (I.e., due to the higher level of heat transferred to the cold particles at the top of the vertical conduit, the walls at the bottom of the conduit will be hotter, resulting in upward free convection or "hot air rising".)

- Subtask 6.1: Establish a new baseline. The particles will be converted from monodisperse to bi-disperse for the most successful geometry found in task 1.

- Subtask 6.2: Relax uniform PSD. The binned uniform PSD will be replaced by a binned normal distribution (Gaussian) and binned skew distributions (e.g., lognormal).

- Subtask 6.3: Introduce particle roughness via estimated size of asperity heights. The impact of this roughness level, which is an input to the heat transfer model, on the heat transfer will be assessed via DEM simulations.

- Subtask 6.4: Make order-of-magnitude estimate of natural convection (buoyancy) forces. NREL estimates for the temperature gradients within the full-scale conduit will be utilized to approximate the free convective flow. The magnitude of the free convective momentum will be compared to the particle momentum simulations described above to assess possible benefit.

Milestone (Task 6) 2/15/2015: The criteria for success in Task 6 expands upon the criteria for Task 5 by requiring that the TAOHTC meet or exceed the target 400 [W/m^2K] for non-radiative mechanisms. Analysis methods will be identical to those previously outlined in Eq. 10-12 above while the simulation configurations for Task 6 are outlined below in the milestone table.

Milestone Table (Task 6)

Variable	**H_{system}**	**% Dev From Baseline**	**% Dev From** *Configuration 3*
PSD 1	201	570	-73
PSD 2	185	516	-76
PSD 3	180	500	-76.5
Surface Roughness 1	770	2467	0
Surface Roughness 2	770	2467	0
Surface Roughness 3	770	2467	0
Calculation of Percent Deviation From Baseline		$= \frac{H_{trial} - H_{baseline}}{H_{baseline}}$	

Project Results and Discussion

The review of results is intended as a high-level overview and representative results. In summary, all of our milestones were met and go/no-go decisions successfully passed. Further detail on the results outlined below can be found in our RPPR reports and are not repeated here due to the space constraints associated with the final report.

YEAR 1

Task 1: Model Verification/Validation for Non-Radiative Heat Transfer

The main objective of the work is to develop a continuum model that can be used for design and optimization of the heat transfer in the proposed solar receiver. We have passed a key milestone towards this goal by using DEM simulations to validate the continuum heat transfer models for conduction and convection. We evaluated the validity of the continuum model for different flow conditions for particles falling over a heated cylinder. As demonstrated in Figure 4, we found that *the heat transfer coefficient predicted by the continuum model is within 8.8% of DEM predictions* when the mass flow rate is high enough such that particles densely pack along the cylinder surface, which is the targeted operating region for the solar receiver. Specifically, the solar receiver in CSP applications is expected to operate in this dense regime to maximize the heat transfer.

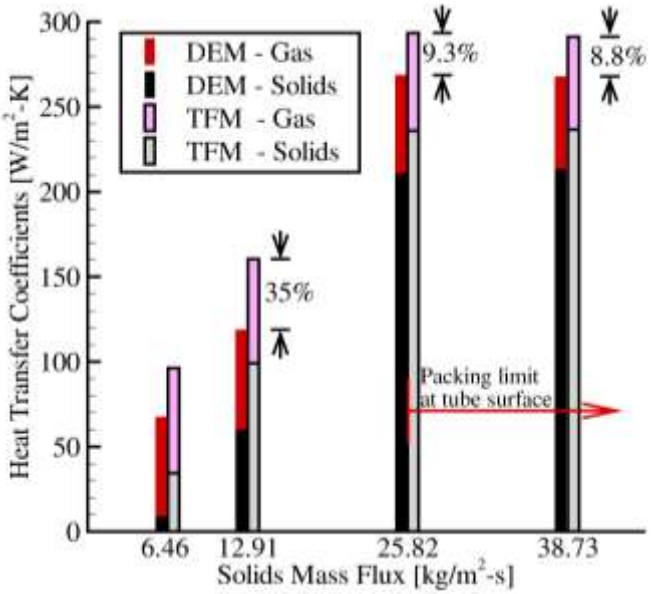

Figure 4. Comparison of heat transfer coefficients for single-tube system where the wall temperature is 800K and the inlet particle temperature is 300K. The "gas" and "solids" in legend refer to convective and conductive mechanisms, respectively.

In addition to generating validation data for the continuum model, a key objective was to use the DEM data to better understand the physics and the mechanisms by which heat is transferred to the particles. Energy can be transferred to the solids phase either directly, i.e. particle-wall or particle-fluid-wall conduction, or indirectly via convective heat transfer with the background fluid. To determine the relative significance of these mechanisms, the case of flow past a heated cylinder was considered. The local heat transfer coefficients this system were obtained and plotted in Figure 5. The particles (500 μm) and gas enter the domain at an inlet solids fraction of 10% and a temperature of 300K, while the tube wall is held at a constant temperature of 800K. The blue line represents heat transfer directly from the tube to the particle phase and the red line represents convective heat transfer to the gas. The solids heat transfer coefficient is large near the stagnation point and diminishes to zero where the particle sheath separates from the surface of the cylinder. The local heat transfer coefficient for direct heat transfer to the solids phase is approximately 5-6 times larger than the heat transfer to the gas phase. At a location 60° from the stagnation point, the heat transfer to the solids phase is equally significant as the heat transfer to the entrained gas. At angles greater than 60°, the particle sheath separates and convective heat transfer to the gas phase dominates.

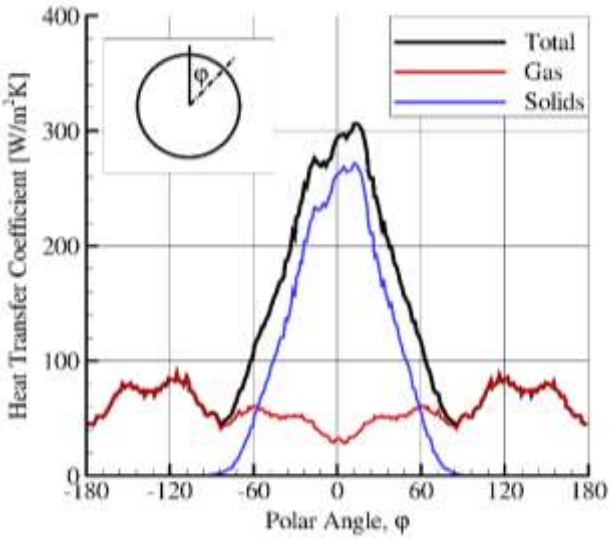

Figure 5. Local heat transfer coefficients for convection to the gas (red line) and conduction to the solids (blue line) for 500µm particles with a mass flow rate of 12.91g/cm^2-s.

The local heat transfer coefficients are plotted in Figure 6 for a higher mass flow rate with an inlet solids fraction of 20% and mass flow rate of 25.82g/cm^2-s. In this regime, the particles are significantly more packed along the top surface of the cylinder and the direct heat transfer to the solids phase is significantly increased. At the stagnation point, the heat transfer to the solids phase is approximately 25 times greater than convective heat transfer from the cylinder to the gas. The particles separate from the surface approximately 60° from the stagnation point, similar to the lower mass flow rate case previously discussed, and convective heat transfer to the gas dominates in the wake of the cylinder. These results show that improvements to the efficiency of the solar receiver can be obtained by using a tube geometry that maximizes particle contact with the heat transfer surfaces.

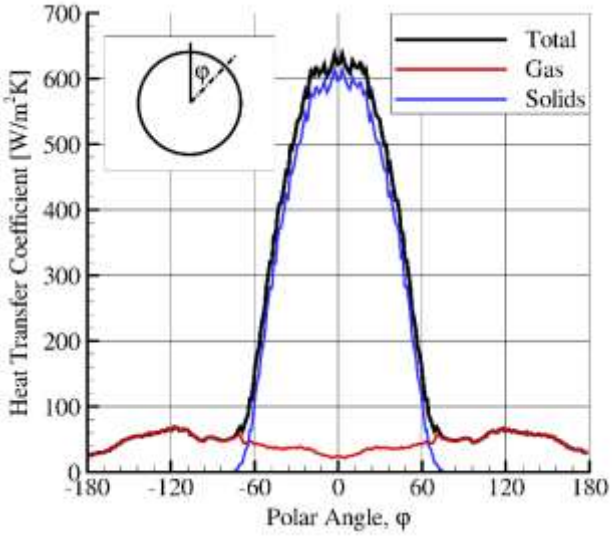

Figure 6. Local heat transfer coefficients for convection to the gas (red line) and conduction to the solids (blue line) for 500µm particles with a mass flow rate of 25.82g/cm^2-s.

The heat transfer directly from wall to solids (blue line in Figures 5-6) can be further decomposed into particle-wall conduction and particle-fluid-wall conduction, as discussed in the background**.** Our DEM simulations show that the latter mechanism dominates whereas direct particle-wall conduction is negligible. For example, the local heat transfer coefficients for particle-wall and particle-fluid-wall conduction are shown in Figure 7. A logarithmic scale is used on the vertical axis to highlight the large differences between the two mechanisms, where particle-fluid-wall conduction transfers more than 100 times as much energy as particle-wall conduction. These results suggest that the accuracy of the simulation can be more efficiently improved by focusing efforts on better modeling conduction through the interstitial gas.

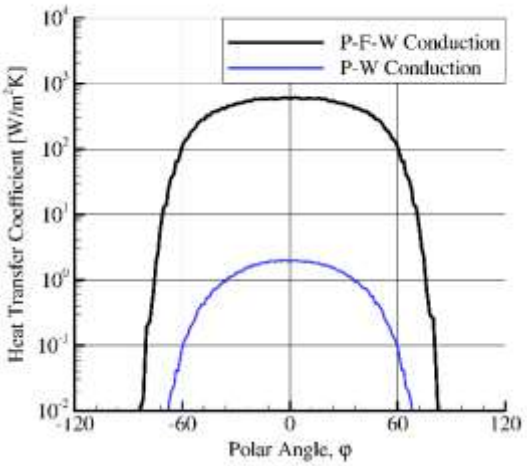

Figure 7. The local heat transfer coefficient for particle-fluid-wall (P-F-W) and particle-wall (P-W) heat transfer. The polar angle is measured from the top stagnation point.

While extending the capabilities of MFIX-DEM to include heat transfer boundary conditions for the particle phase (above), we have also improved the utility of MFIX-DEM by parallelizing the heat transfer algorithms, enabling us to perform these simulations on supercomputers at ORNL (Titan) and the University of Colorado Research Center (Janus). Examples of scalability on both platforms is indicated in Figure 8.

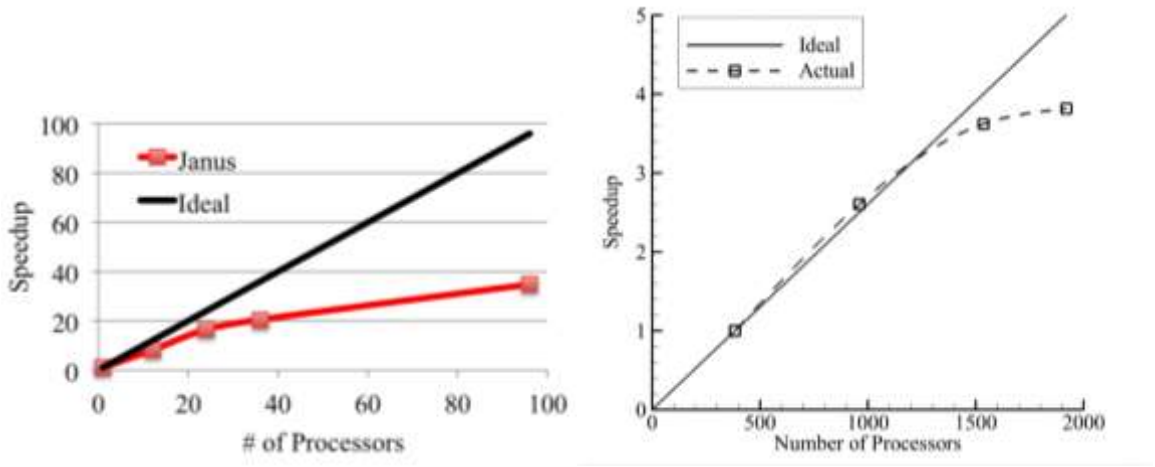

Figure 8. The parallel scalability of MFIX-DEM on Janus (left) and Titan (right).

Task 2: Initial Assessment of MFIX Radiation Model

We have documented the current state of the radiation models in MFIX-DEM and the continuum model in Section 6 of the Year 1 Continuation Report. In summary, a new radiation model has been implemented into the continuum framework for MFIX [28]. This radiation model solves an approximate form of the radiative transfer equation and has been tested by its developers for spouted bed simulations. For the MFIX-DEM model, the radiative heat transfer is simplified by assuming that for each particle, the neighboring particles form a spherical shell with a single "environment" temperature. The environment temperature depends on the nearby particle temperatures within the spherical shell and the size of the shell is assumed to be 1.5 particle diameters. This reduces the challenge of computing view factors for all particle pairings by simplifying the transfer to one particle to a concentric sphere. We have not found evidence in the literature that the MFIX continuum radiation models have been validated by comparison to analytic solutions for radiation in a participating media.

YEAR 2

Task 3: Validation of Hydrodynamics and Heat Transfer Model for Hexagonal Array

The objective of this task is to develop and validate a continuum heat transfer model that accurately predicts the heat transfer in a solar receiver with hexagonal tubes over a robust range of system parameters. A schematic of the hexagonal geometry simulated is provided in Figure 9 and the effect of horizontal spacing on the local heat transfer results (via DEM simulations) is depicted in Figure 10. The new continuum model is fundamental (it only relies on measured properties, not empirical parameters) and the heat transfer depends on particle size, morphology, solids concentration, and thermal properties of the interstitial gas. A rigorous derivation of the model and assessment of accuracy is discussed in the Continuation Report for Year 2, the significant contributions section, and was published in the *International Journal of Heat and Mass Transfer*. This model was used for the simulated solar receiver and the heat transfer comparisons vastly

improve on existing state of the art models. An example of the continuum-DEM comparison that serves as validation for the new continuum model is given in Figure 11. The results over the whole range of parameters examined are summarized in Milestone Table for Task 3 (see previous section).

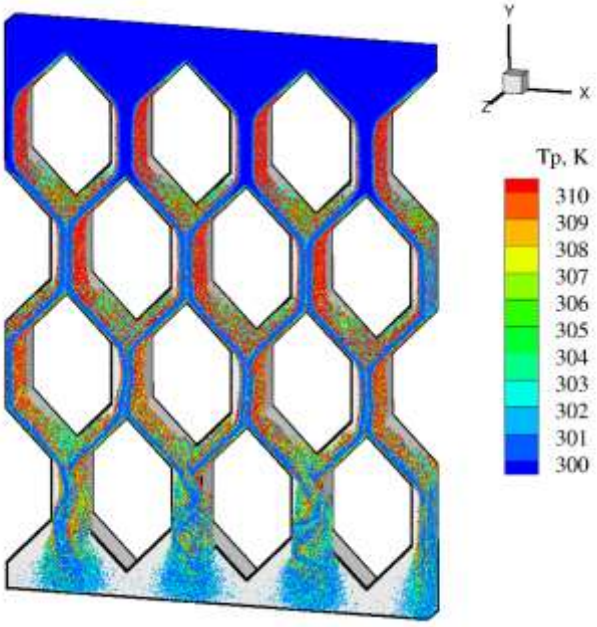

Figure 9. 3-D DEM simulations showing particles colored by thermal temperature flowing through a hexagonal tube array.

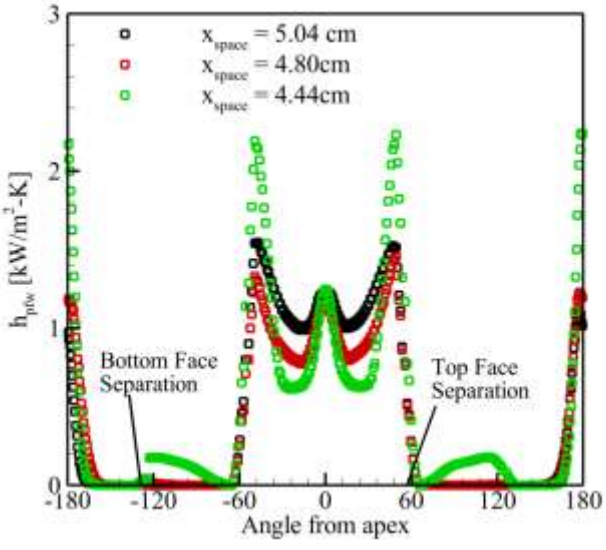

Figure 10. Local heat transfer coefficient for solids conduction along the surface of a hexagon in the 2nd row of the array. Different colored symbols correspond to different horizontal spacing.

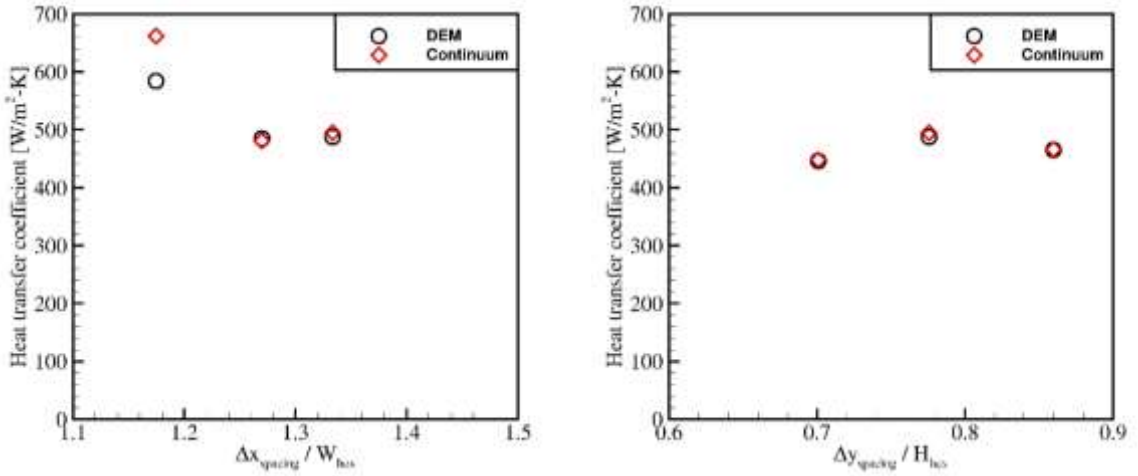

(a) *(b)*

Figure 11. Total heat transfer coefficient by the new model compared to DEM for (a) the x-spacing (normalized by hexagon width) and (b) the y-spacing (normalized by hexagon height).

In summary, all milestones associated with Task 3 were accomplished, as listed below.

1. The average error in the heat transfer coefficient predicted by the continuum model is 5.7%, less than the 20% cutoff specified in the go/no-go criterion.

2. T-value test shows that the confidence interval for the continuum model having an error less than 20% is 99.9935% and exceeds the 95% required confidence interval.

3. A paper on the new continuum heat transfer model was published in the *International Journal of Heat and Mass Transfer.*

4. A paper discussing DEM simulations and the continuum heat transfer model predictions for particles flowing through the solar receiver was published in *Solar Energy*.

Finally, the requested go/no-go figures are summarized below in Figures 12-14. The Nusselt number is defined as

$$Nu = \frac{\bar{h}_{tot} W}{\kappa_g} \quad \bar{h}_{tot} = \frac{Q_{tot}}{\sum_{N_{hex}} A_{hex}}, \tag{13}$$

where h_{tot} is the total heat transfer coefficient, Q_{tot} is the total heat transfer rate for the system, W is the width of a hexagon, κ_g is the gas thermal conductivity, A_{hex} is the surface area of a hexagon, and N_{hex} is the number of simulated hexagons. The Nusselt number is directly proportional to the heat transfer coefficient, but additional discussion of the Nusselt number plots will be reserved for the RPPR reports.

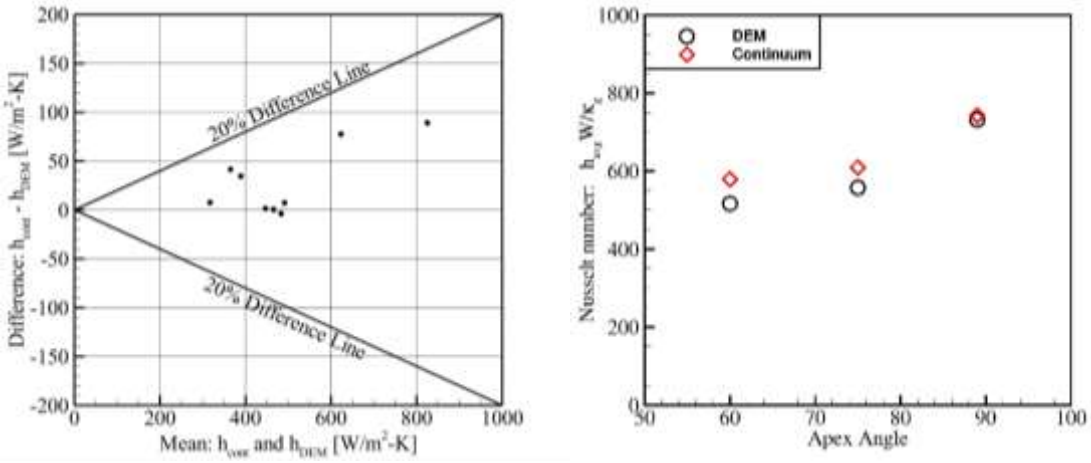

Figure 12. Tukey mean-difference plot (left). Nusselt number dependence on apex angle (right).

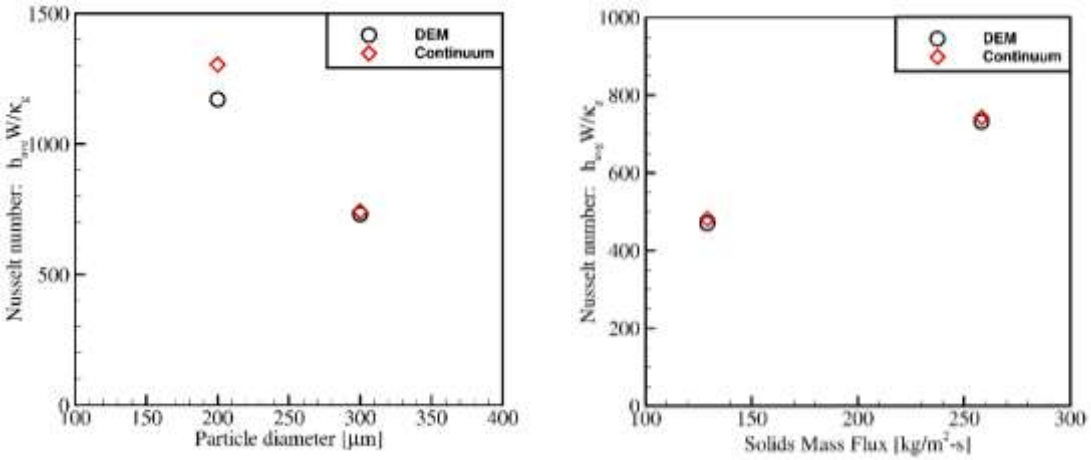

Figure 13. Nusselt number dependence on (left) particle diameter and solids mass flux (right).

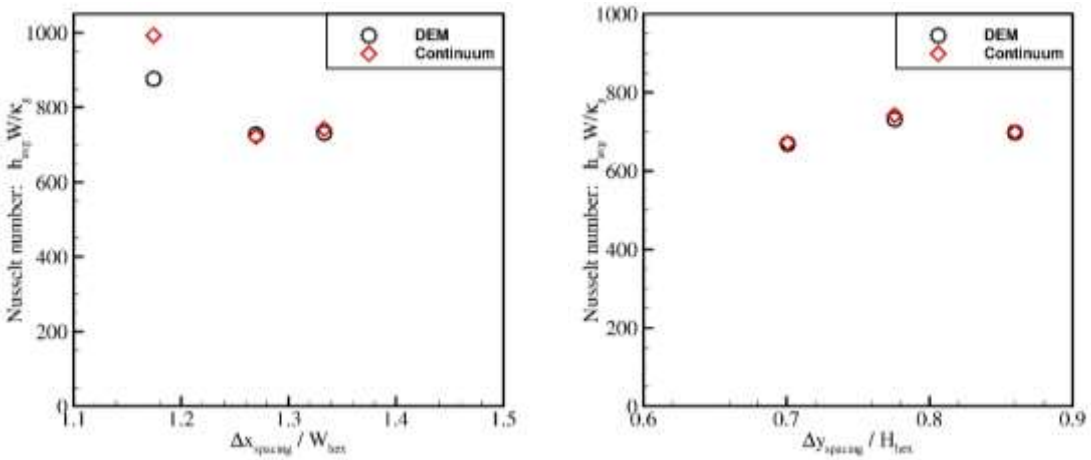

Figure 14. Nusselt number dependence on (left) horizontal gap and (right) vertical gap spacing.

Task 4: Comparison of DEM and continuum models to laboratory scale

Since data from experiments at NREL and The Colorado School of Mines only became available as part of the mid-year review, it was decided to forego comparisons to experimental data and focus on Contingency Task 4B. We completed additional simulations for apex angles of 70 and 80°; see Figure 15. The goal from studying the apex angle was to determine whether there were heat transfer benefits associated with having smaller apex angles (more pointed hexagons). The simulations for this task show that although steepening the apex angle increased the flow rate, the overall heat transfer was reduced. The total heat transfer coefficient decreases as the apex angle decreases because the solids concentration near the heated surfaces decrease for sharper apex angles. These observations are consistent with what was found in DEM simulations previously discussed, and the benefits of improved flow rate do not seem to favorably improve the heat transfer in ways similar to that of a traditional molecular fluid.

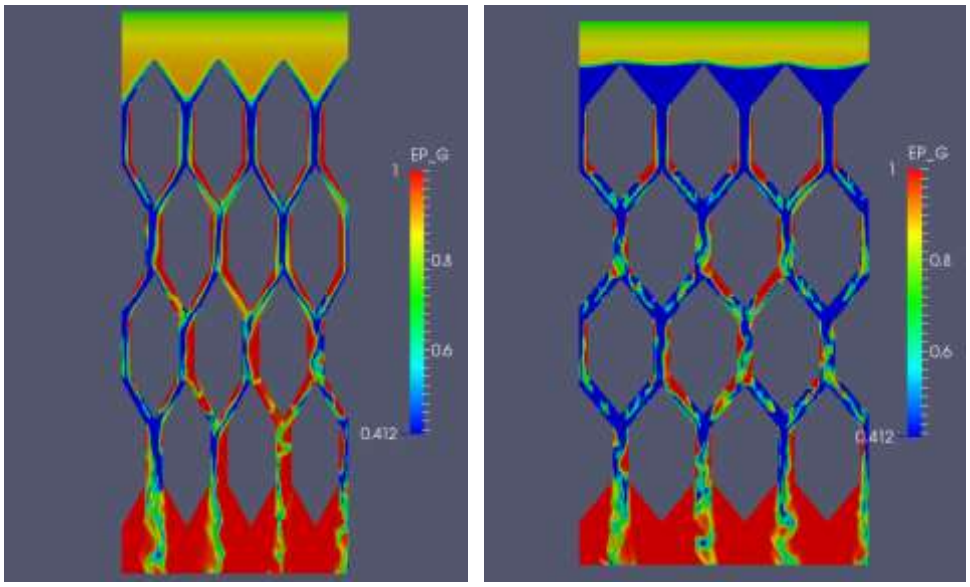

Figure 15. Contours of void fraction for continuum simulations where the apex angle is 70° (left) and 80° (right).

YEAR 3

Task 5: Enhancement of heat transfer for gas-solid flow within a vertical conduit: geometric configuration and mild fluidization

The array of heat exchanger tubes explored in year two (Figure 1, 9, and 15) ultimately proved to be an infeasible design for the near black body receiver. The large disparity in solids heat transfer between the top and bottom of the hexagonal tubes (Figure 10) leads to excessive wall temperature gradients and an inefficient use of conduction area. To address these issues, a new receiver design was developed for year three. The new design (Figure 16 (right)) entails a vertical conduit with alternating internal baffles and a gravity driven gas-solids inflow. With the vertical conduit design, the solar flux will be irradiated upon the conduit; and thus, the emphasis for solids heat transfer is shifted from the flow obstructions (baffles or previously, hexagonal tubes) to the domain walls. For Task 5, the heat transfer within the new receiver design was simulated and the sensitivity to geometric parameters was explored. The thermodynamic and simulation inputs can be found below in Table 5.

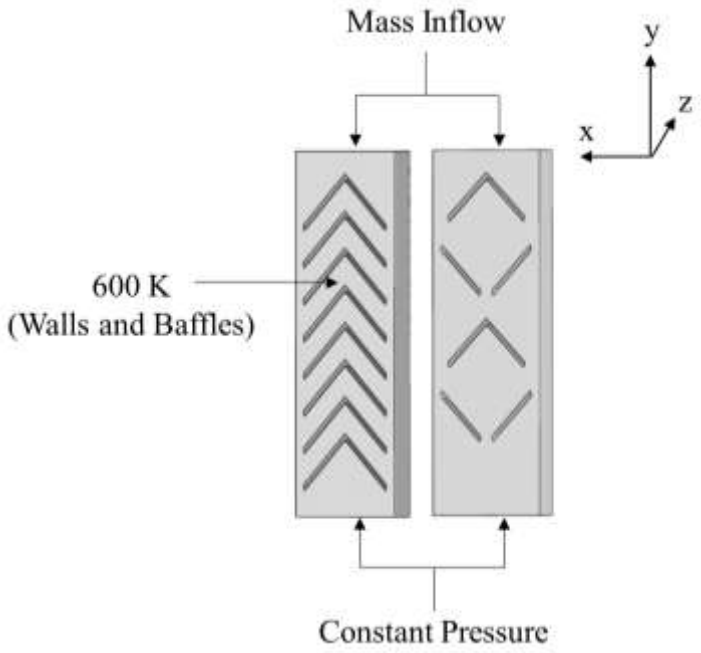

Figure 16. (left) The improved baffle geometry (Configuration 3) and (right) the original baffle geometry (Configuration 1) for the new receiver design.

Table 5: Simultion Inputs

Species: Air			
ρ_g	$\rho_g = \frac{P_g Mw}{RT_g}$	$Mw = 28.97\ \frac{kg}{kmol}$	
K_g	$K_g = K_{g,ref}\sqrt{\frac{T_g}{T_{g,ref}}}$	$K_{g,ref} = 0.0252\ \frac{W}{m\ K}$	$T_{g,ref} = 300\ K$
$C_{p,g}$	$1.0042\ \frac{kJ}{kg\ K}$		
μ_g	$\mu_g = \mu_{g,ref}\left(\frac{T_g}{T_{g,ref}}\right)^{\frac{3}{2}}\left(\frac{T_{g,ref}+S}{T_g+S}\right)$		
	$\mu_{g,ref} = 1.72 * 10^{-5}\ Pa\ s$	$S = 110.4\ K$	$T_{g,ref} = 300\ K$
Species: Sand (SiO_2)			
$\rho_{p,i}$	$2582\ \frac{kg}{m^3}$		
$K_{p,i}$	$1.402\ \frac{W}{m\ K}$		
$C_{p,i}$	$0.79496\ \frac{kJ}{kg\ K}$		
$d_{p,i}$	$200\ \mu m$		
Boundary Conditions			
Mass Flux	$180\frac{kg}{m^2\ s}$	$\varepsilon_s = 0.50$	
$T_{g/s,inlet}$	$300\ K$		
$P_{g,outlet}$	$101.325\ kPa$		
$T_{wall,baffles}$	$600\ K$		

Simulation of the new receiver design (Configuration 1) was expected to yield good solids heat transfer throughout the entire domain. It had initially been hypothesized that the alternating converging and diverging baffles would promote mixing and force particle-wall contacts. However, as the hydrodynamic and heat transfer data (Figure 17) show, the resulting overall system heat transfer coefficient (78 $[W/m^2K]$) is well below the target (320 $[W/m^2K]$). Close inspection of the hydrodynamic profile for Configuration 1 (Figure 17 (a)) shows that low solids concentrations persist throughout the system, and particularly after converging baffles. Since the particle conduction mechanisms are primarily a function of particle-wall proximity, low solids concentrations result in a low number of particle-wall contacts, and thus, low solids heat transfer. To avoid regions of high void fraction, the particles must be consistently forced into contact with

the walls. Therefore, a geometry change was made to remove the converging baffles in lieu of only diverging type baffles. In addition, the vertical spacing between baffles was reduced to maintain more uniform contact.

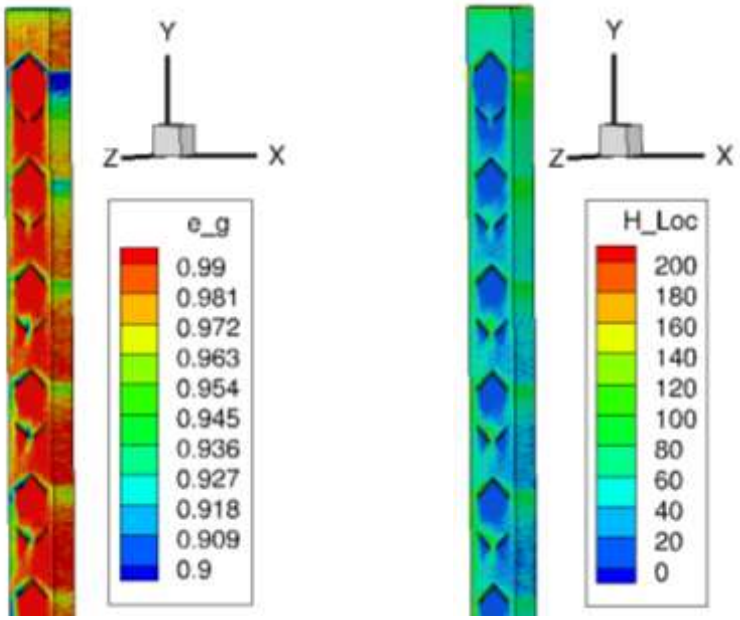

(a) *(b)*

Figure 17. Baffle Configuration 1: (a) Gas fraction (e_g) and (b) local heat transfer coefficients (H_Loc) $[W/m^2K]$.

Implementation of the aforementioned geometry changes resulted in a marked increase in the overall system heat transfer coefficient (215 $[W/m^2K]$). However, it was still believed that the solids fractions were too low near boundary walls. From previous work with gravity driven flows, it was known that solids at the inlet of the simulation begin to accelerate under the force of gravity and cause the void fraction to increase exponentially as fall height increases. In addition, void fraction profiles as a function of fall height are strongly related to initial conditions. Therefore, by increasing the solids fraction at the simulation inlet, it was hypothesized that the dilution of particles before contact with the first baffle could be reduced. Hydrodynamic, heat transfer, and solids temperature results for this final improved geometry (Configuration 3) are shown below in Figure 18 below. The compounding of configurational modifications yielded an overall heat transfer coefficient of 601$[W/m^2K]$. Time averaging of the overall heat transfer coefficient for Baffle Configuration 3 between 0.60000-0.66427[s] led to a time average overall heat transfer coefficient (TAOHTC) of 592, a standard deviation of 14.2, and a sample size of 6. From Eq. 12, it follows that, with 95% confidence, the TAOHTC is statistically greater than 400 ($-11.7 <$ 192). Furthermore, by altering the target value to force the left side of Eq. 12 equal to the right side yields an upper bound for the TAOHTC, which is 603$[W/m^2K]$.

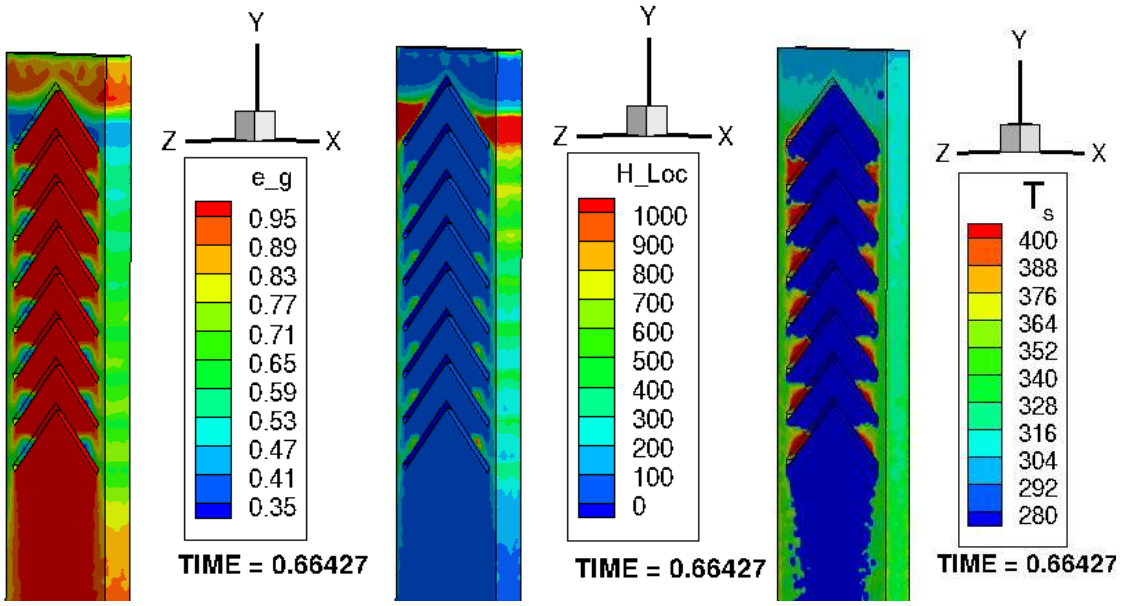

(a) *(b)* *(c)*

Figure 18. Baffle Configuration 3: (a) Gas fraction (e_g), (b) local heat transfer coefficients (H_Loc) $[W/m^2K]$, and (c) solids temperature (T_s) [K].

The effect of baffle apex angle upon the system heat transfer coefficient was explored once a new baseline had been developed (Configuration 3 above). It should be noted that while the baffles significantly contribute to the heat transfer in the simulations, they are not the intended main source of heat transfer in the real system. Therefore, the focus for enhancing heat transfer should be placed upon the domain walls and not the baffles. *When altering the baffle apex angle, it was found that the heat transfer with the domain walls was not a strong function of apex angle but that the heat transfer with the baffles was.* Specifically, that more obtuse baffle angles led to higher baffle heat transfer coefficients due to enhanced particle-baffle contacts. The heat transfer results from simulating systems with baffle apex angles of 45°, 36°, and 30° are summarized below in Figures 19-20.

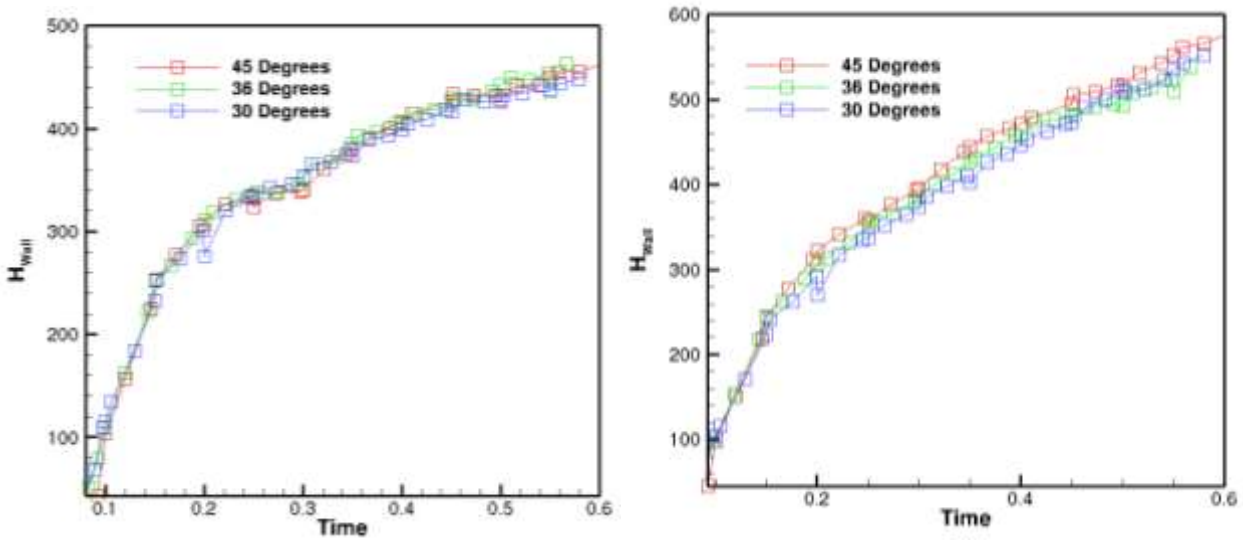

(a) (b)

Figure 19. (a) The average heat transfer coefficient for the East XY plane wall for all apex angles simulated. (b) The average heat transfer coefficient for the West XY plane wall for all apex angles simulated.

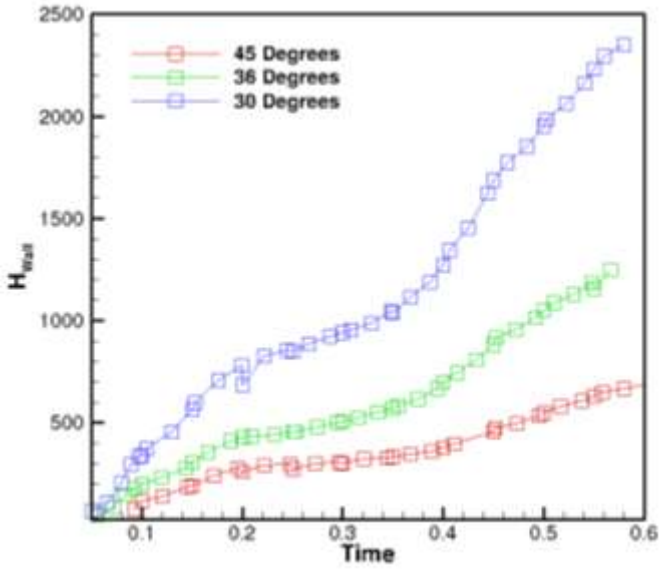

Figure 20. The average heat transfer coefficient for all baffles during the apex angle simulations.

Task 6: Enhancement of heat transfer for gas-solid flow within a vertical conduit: particle properties (size distribution and roughness) and free convection

The effect of particle size distribution on heat transfer was explored by converting the monodisperse solids to a bi-disperse mixture. The volume fraction of both solid phases was allowed to vary so that different effective diameters for the mixture could be achieved. Specifically, the following particle size distributions were simulated with the Configuration 3 geometry.

1. Skew high distribution ($d_{p,eff} = d_{p,1}\frac{\varepsilon_{s,1}}{\varepsilon_{s,1}+\varepsilon_{s,2}} + d_{p,2}\frac{\varepsilon_{s,2}}{\varepsilon_{s,1}+\varepsilon_{s,2}} = 237.5\ \mu m$)
    a. $d_{p,1} = 250\ \mu m \quad \varepsilon_{s,1} = 0.09$
    b. $d_{p,2} = 125\ \mu m \quad \varepsilon_{s,2} = 0.01$
2. Even distribution ($d_{p,eff} = 187.5\ \mu m$)
    a. $d_{p,1} = 250\ \mu m \quad \varepsilon_{s,1} = 0.05$
    b. $d_{p,2} = 125\ \mu m \quad \varepsilon_{s,2} = 0.05$
3. Skew low distribution ($d_{p,eff} = 137.5\ \mu m$)
    a. $d_{p,1} = 250\ \mu m \quad \varepsilon_{s,1} = 0.01$
    b. $d_{p,2} = 125\ \mu m \quad \varepsilon_{s,2} = 0.09$

It should be noted that the solids volume fraction ($\varepsilon_{s,1} + \varepsilon_{s,2}$) at the inflow boundary was reduced from 0.5 (Configuration 3 monodisperse) to 0.1. The need for a larger void fraction at the column inlet is due to two numerical factors. First, soft-sphere DEM resolves each particle collision over time; and therefore, the solids time step decreases with particle size ($\Delta t \propto d_p^{-3}$). Since collisions between different size particles are permitted, the system time step is governed by the smallest particle. I.e., introduction of the 125 μm particle forced the solids time step to decrease by nearly an order of magnitude. Second, as the particle size decreases, the total number of particles in the system increases (for a constant mass inflow). The high number of particles creates a large overhead for processor memory and further inhibits simulation progress. Since the polydisperse simulations required inflow conditions that differed from their monodisperse analog, a monodisperse Configuration 3 was simulated with the same solids fraction ($\varepsilon_s = 0.1$) as the polydisperse cases.

The void fraction profiles resulting from simulation of the monodisperse (Configuration 3 with $\varepsilon_s = 0.1$) and polydisperse cases are given in Figure 21 below. A general hierarchy is observed in the solids fractions near the wall: monodisperse > skew high > even ≅ skew low. Since the particle conduction mechanisms are strictly governed by particle-wall proximity, the same trend is observed for heat transfer (Figure 22 below).While it had been expected that a polydisperse solids phase would lead to greater heat transfer, due to higher packing fractions, the monodisperse case exhibits the largest overall heat transfer coefficient. The observed trends can be attributed to one physical and one numerical factor. The physical effect is that granular flows through a constriction will experience less impedance as the constriction to particle diameter ratio increases. As the solids fraction of the 125 μm particle is increased, the effective diameter of the mixture decreases and the solids can pass through the baffle-wall gap with greater ease. The numerical effect is caused by variances in the mass inflow that arise from seeding different sized particles. Specifically, new particles must be seeded along the inflow plane in a manner than prevents overlap. Therefore, the amount of time between seeding events is dictated by the largest particle

diameter (particle must completely clear the inflow plane). While this method ensures that particles do not overlap, it leads to a larger seeding time constant than is necessary. When seeding a new particle in a position that was previously occupied by a smaller particle, the smaller particle has not only passed the inflow plane but propagated into the domain some finite distance. The reduction in mass inflow arising from the polydisperse inflow will ultimately be detrimental to the system heat transfer.

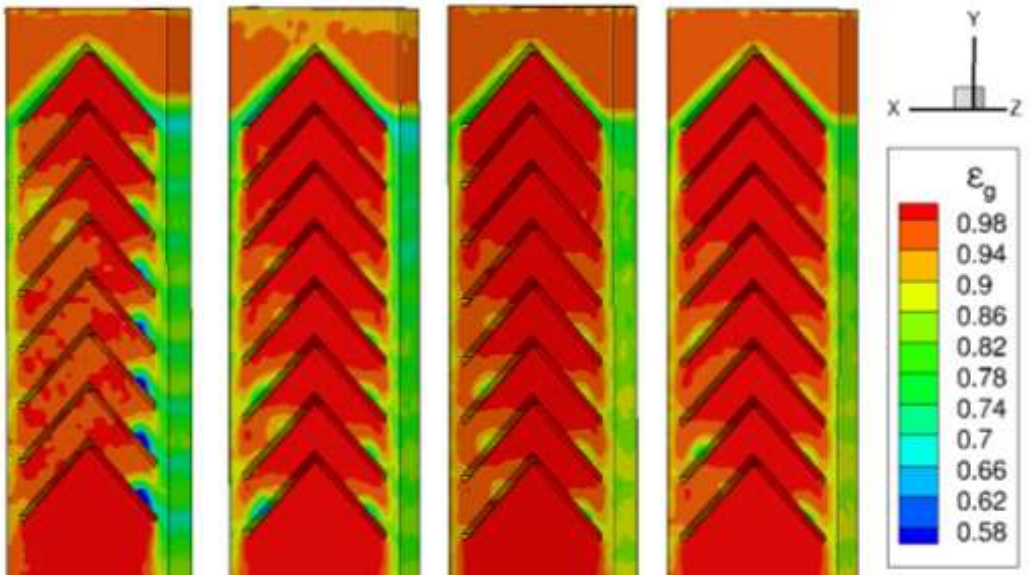

(a) *(b)* *(c)* *(d)*

Figure 21. Gas volume fraction profiles for the monodisperse (a), skew high distribution (b), even distribution (c), and skew low distribution (d).

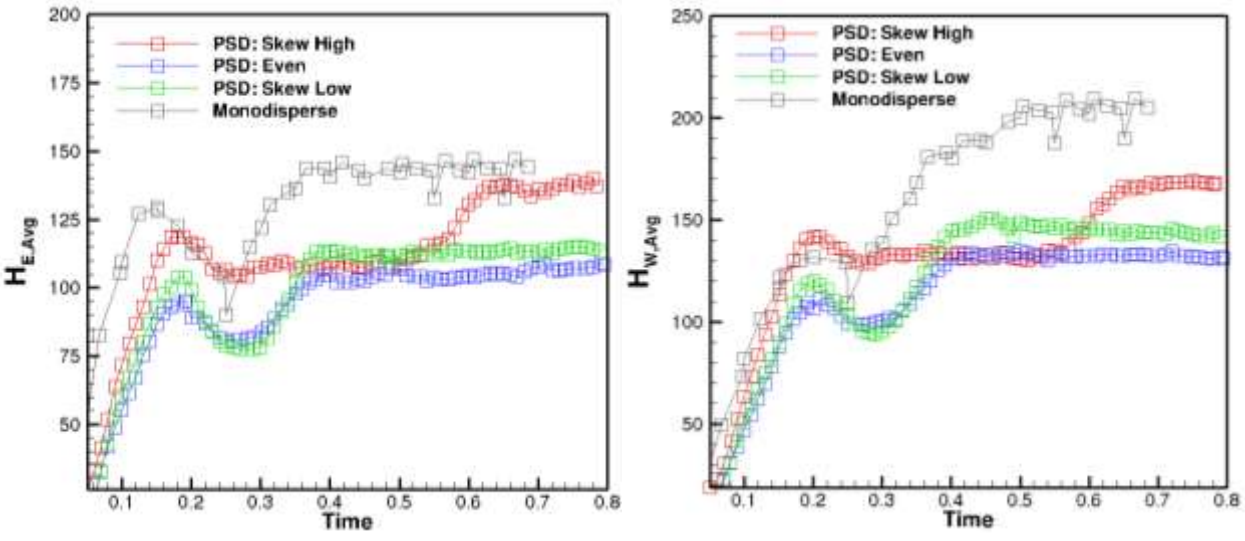

(a) *(b)*

Figure 22. The average heat transfer coefficient along the eastern (a) and western (b) wall as a function of simulation time and particle size distribution.

As described in the background section, the particle roughness is a direct input into the static fluid lens model (minimum conduction distance) and was taken to be the mean free path of the gas (S=27.5 nm) in all previous simulations. Work with *single-particle* systems suggests that the lens model may be insensitive to the lens thickness but have a strong dependence upon the minimum conduction distance [20], with larger minimum conduction distances reducing the particle-wall heat transfer. To gauge the sensitivity of Configuration 3 (a *monodisperse multi-particle* system) to particle roughness, the minimum conduction distance was set according to laboratory measurements of average particle asperity heights (S=50, 100, 200 nm). The average heat transfer coefficients for all three roughness values are given below in Figure 23-24 for the East/West walls and the baffles (respectively). *By contrast to the static single-particle results, it is found that dynamic multi-particle systems are insensitive to the minimum conduction distance.* A physical explanation can be found by considering the analytical solution to the non-dimensionalized static fluid lens model (Eq. 14) and the particle-wall distribution function (Figure 25):

$$\hat{H}_{pfw} = \frac{H_{pfw}}{K_g R_p} = 2\pi \left[\left(\hat{\delta}+1\right) Ln \left[\frac{\left| \sqrt{1-\hat{R}_{max}^2} - \left(\hat{\delta}+1\right) \right|}{\left| \left[\hat{\delta}+1\right] - \sqrt{1-\hat{R}_{min}^2} \right|} \right] - \sqrt{1-\hat{R}_{min}^2} + \sqrt{1-\hat{R}_{max}^2} \right] \quad (14)$$

where R_p is the particle radius, $\hat{\delta} = \delta / R_p$ is the non-dimensional particle-wall separation distance, K_g is the gas thermal conductivity, $\hat{R}_{min} = R_{min}/R_p$ is the non-dimensional lower bound of integration (depends upon the minimum conduction distance), $\hat{R}_{max} = R_{max}/R_p$ is the non-dimensional upper bound of integration (point of intersection between the lens and wall), and $\hat{H}_{pfw}$ is the non-dimensional heat transfer coefficient for the particle-fluid-wall mechanism. For a multi-particle system, the sensitivity to an input parameter can then be approximated by the weighted average of the difference between two analytical solutions by the particle-wall distribution function:

$$\%Error = \frac{\int_{\hat{R}_{min}}^{\hat{R}_{max}} \chi_{(\hat{\delta})} \left[\hat{H}_{pfw,1} - \hat{H}_{pfw,2} \right] d\hat{\delta}}{\int_{\hat{R}_{min}}^{\hat{R}_{max}} \chi_{(\hat{\delta})} \hat{H}_{pfw,1} d\hat{\delta}} \quad (15)$$

where $\chi_{(\hat{\delta})}$ is the particle-wall distribution function given in Figure 25. Physically, the above calculation method weights the difference between two heat transfer closures by the probability of a particle being located at that distance away from the wall. Since the minimum conduction distance only affects the analytical solution when the separation distance is less than the minimum conduction distance ($\delta < s$), error only occurs when $\delta \in [0, s]$ (particle is essentially in contact with the wall). Direct calculation via Eq. 15 yields percent errors less than 1% for all roughness values simulated. However, if the impact of the fluid lens thickness is examined, a very different result is achieved. The deviation in analytical solutions for two fluid lens thicknesses (40% and 20% the particle radius) is given in Figure 26 (a). For the case of a varying lens thickness, a deviation in analytical solutions occurs over all separation distances, and results in non-negligible error (Figure 26 (b)). A numerical test of the previous prediction (point in Figure 26 (b)) shows reasonable agreement between the expected error and the observed error. *In summation, the heat transfer of a monodisperse, dynamic, multi-particle system due to indirect conduction is found to*

not be a strong function of minimum conduction distance but does strongly depend upon the fluid lens thickness.

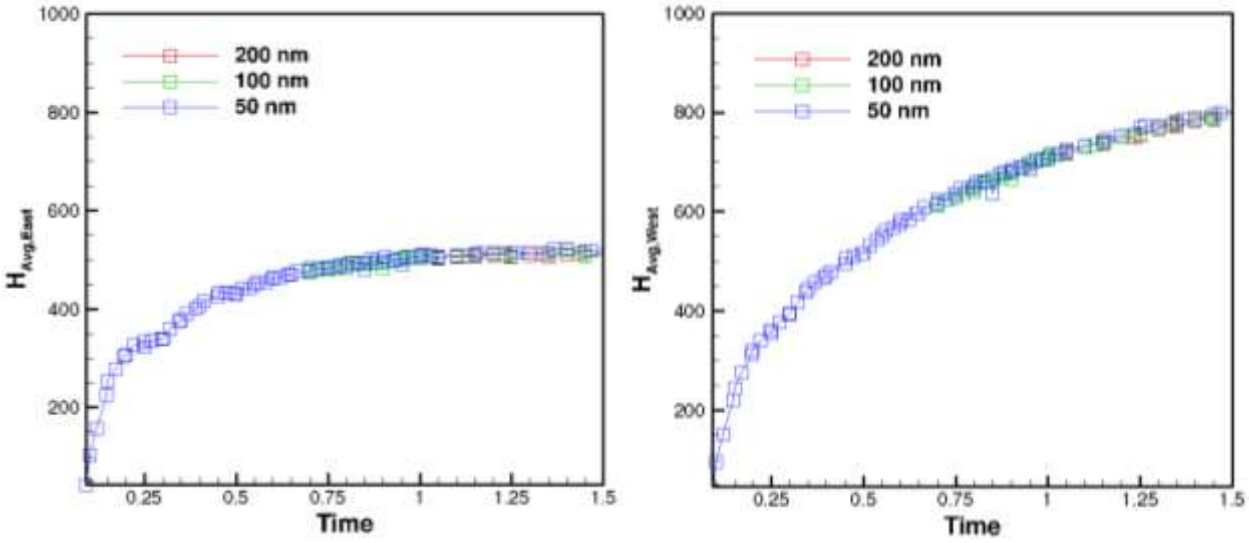

(a) *(b)*

Figure 23. The average heat transfer coefficient along the eastern (a) and western (b) wall as a function of simulation time and particle roughness.

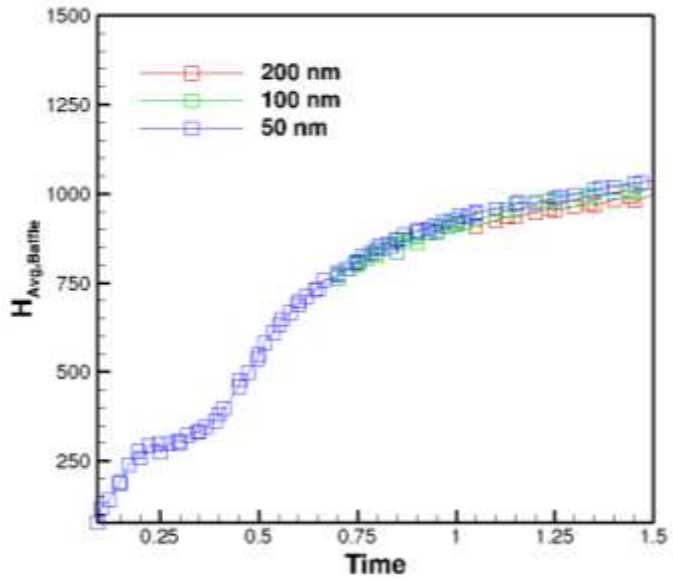

Figure 24. The average heat transfer coefficient for all baffles as a function of time and particle roughness.

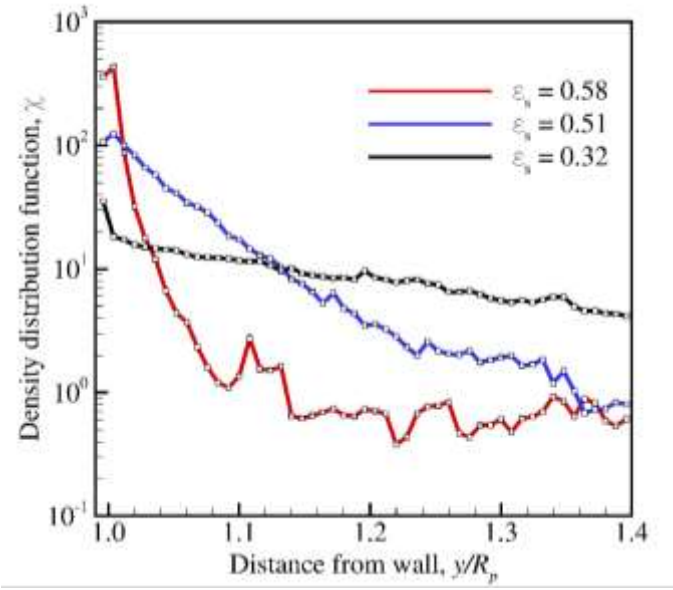

Figure 25. The particle wall distribution at varying solids fractions found during year 2.

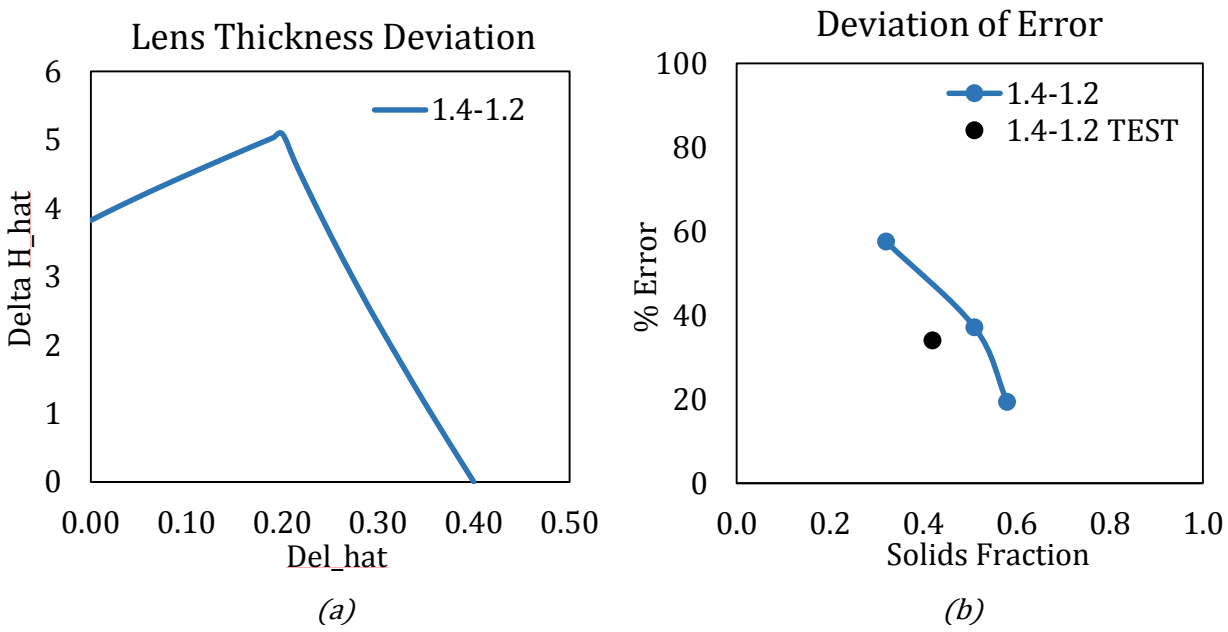

Figure 26. (a) The deviation between analytical solutions for two lens thicknesses (40% and 20% of the particle radius). (b) The predicted error between calculation methods is compared with a numerical test.

Significant Accomplishments and Conclusions

As outlined in the project objectives, the tasks of developing a new continuum heat transfer model (Subtask 3.1) and thermal boundary condition (Subtask 6.4) were undertaken. These two advancements build upon the current state-of-the-art for multiphase heat transfer and allow critical results to be ascertained. While the DEM methodology was briefly discussed in the background section, the restrictions to system size were not delved into. Namely, simulations are generally restricted to $\mathcal{O}(10^6)$ particles. The tracking of properties for each discrete particle (position, velocity, temperature, etc.) poses a significant memory overhead, while the resolution of particle collisions (soft-sphere method) necessitates the use of small time steps. In order to simulate industrially relevant systems, a continuum framework must be employed (TFM). For this reason, the development of a continuum heat transfer model from first principles, which accurately predicts particle size dependence, is of great significance. We were successful in developing said model, and a detailed description of it can be found below, along with comparisons to DEM results. The importance of wall temperature gradients was also briefly discussed above (Year 3 project results). Unfortunately, the prediction of wall temperatures, arising from a multiphase flow experiencing a constant heat flux, poses a significant challenge to both DEM and TFM frameworks. Specifically, a constant heat flux boundary condition was not available for DEM, while a constant flux to each phase must be specified in TFM. Practically speaking, the receiver is most properly described by a constant flux to the entire gas-solid mixture, with varying heat fluxes to each phase. We have developed a new thermal boundary condition which satisfies the aforementioned description, and is also described in detail below.

Continuum Heat Transfer Model

To transition from the individual particle heat fluxes in DEM to a continuum heat flux, the contribution from all particles undergoing conduction must be accounted for. Therefore, the positions of all particles relative to the wall are required. The particle-wall distribution function χ is defined as the probability that a particle center exists within a distance y to $y+dy$ from the wall. This distribution function is analogous to the radial distribution function which is commonly used in the kinetic-theory-based models to correlate contacts between particles [15]. A schematic showing the particle-wall distribution function is shown in Figure 27.

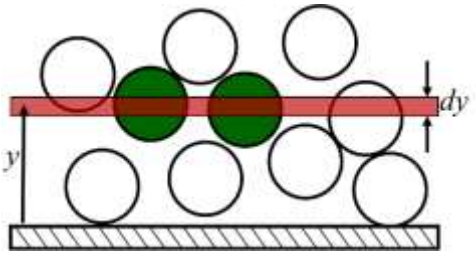

Figure 27. Schematic of particle-wall distribution function with two green particles whose centers lie within a distance y to y+dy from the wall.

The continuum heat flux is obtained by coupling the single particle conductance with the particle-wall distribution function χ, and integrating from those particles in contact with the surface, $\delta = 0$, to a distance where the particle fluid no longer intersects the wall, $\delta = 1-R_{lens}$.

$$q''_{pfw} = \frac{\dot{Q}_{pfw}}{A} = h_{pfw}\left(T_w - T_p\right) = n_p R_p \kappa_g \left(T_w - T_s\right) \frac{\int_0^{1-\hat{R}_{lens}} \chi\left(\hat{\delta}\right)\hat{H}\left(\hat{\delta}\right) d\hat{\delta}}{\int_0^{1-\hat{R}_{lens}} \chi\left(\hat{\delta}\right) d\hat{\delta}} \tag{16}$$

The variable n_p is the number of particles that are within the particle lens thickness of the wall per unit (wall) area, A. The particle-fluid-wall local heat transfer coefficient is defined as h_{pfw}. The integrand in the numerator is the contribution to the heat flux from particles that are within a distance δ to $\delta+d\delta$ from the wall. The integral in the denominator is used to normalize the particle-wall distribution function so that the cumulative probability is unity. Note that the particle temperature, T_p, has been replaced with the continuum solids phase temperature, T_s, and assumed to be constant over the range of integration.

The particle-wall distribution function is not explicitly known for continuum simulations of a particle flow, but this distribution function can be obtained from DEM simulations. However, for the new heat transfer model, Eq. 16, to be useful in a continuum framework, the new particle-wall distribution function must be expressed in terms of continuum variables rather than be obtained from DEM of the system of interest. To close the wall distribution function, it is hypothesized that the particle-wall distribution function is only a function of the solids concentration. Many DEM simulations with different parameters show that the Nusselt number

$$\mathrm{Nu} = \frac{h_{pfw} D_p}{\kappa_g} = \frac{1}{2} D_p^2 n_p \frac{\int_0^{1-\hat{R}_{lens}} \chi\left(\hat{\delta}\right)\hat{H}\left(\hat{\delta}\right) d\hat{\delta}}{\int_0^{1-\hat{R}_{lens}} \chi\left(\hat{\delta}\right) d\hat{\delta}} \tag{17}$$

collapses versus solids concentration, and that the number of particles adjacent to the surface, n_p, is approximated by:

$$n_p = \frac{1}{D_p^2}\left(\frac{\varepsilon_s}{\varepsilon_{s,\max}}\right)^{\frac{2}{3}}, \tag{18}$$

where $e_{s,max}$ is the solids concentration at maximum packing. These assumptions enable one to define a Nusselt number, shown in Eq. 17, which is primarily a function of solids concentration and parameters such as the minimum conduction distance and lens radius. The minimum conduction distance and lens radius are implicitly embedded in the particle-wall conductance terms $\hat{H}$. Although the expression for n_p is approximated by Eq. 18, similar collapse of the Nusselt number can be obtained for any expression for n_p that follows a similar function form of $n_p = f\left(e_s\right)/D_p^2$.

$$\mathrm{Nu} = \frac{1}{2}\left(\frac{\varepsilon_s}{\varepsilon_{s,\max}}\right)^{2/3} \frac{\int_0^{1-\hat{R}_{lens}} \chi\left(\hat{\delta}\right)\hat{H}\left(\hat{\delta}\right) d\hat{\delta}}{\int_0^{1-\hat{R}_{lens}} \chi\left(\hat{\delta}\right) d\hat{\delta}}. \tag{19}$$

The maximum value of the Nusselt number is shown in Eq. 20 and corresponds to maximum packing and a particle-wall distribution function with all particles in contact

$$\mathrm{Nu}_{\max} = \frac{1}{2}\hat{H}\left(0\right). \tag{20}$$

As previously noted, the variable $\hat{H}$ depends on the assumed lens thickness and minimum conduction distance. To reduce these dependencies from Eq. 19, the Nusselt number is normalized by the maximum value of the Nusselt number evaluated using the specified minimum conduction distance and fluid lens radius. When cast in this form, the normalized Nusselt number is primarily a function of solids concentration and is shown in Figure 28 for a set of DEM simulations of particle flow along an inclined plane.

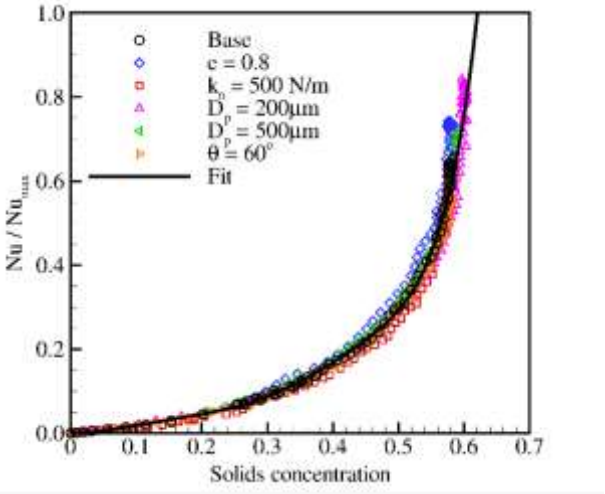

Figure 28. Scaling relationship between the Nusselt number, normalized by the theoretical maximum, and solids concentration. Symbols are 3-D DEM simulations with various flow and model parameters.

The normalized Nusselt numbers collapse very well over the complete range of solids concentrations and flow parameters. The base case simulation in Figure 28 is characterized by 300 μm particles flowing down a ramp inclined 45°. The LSD spring constant and coefficient of restitution were k_n =100 N/m and e = 0.9, respectively, for the base case. Although not all cases are shown, the data collapse well for particle diameters ranging from 200 to 500 μm, inclination angles varying from 30° to 60°, LSD spring constants from 100 to 500 N/m, and for simulations with different mass inflow. The restitution was parametrically varied from 0.7 to 0.95. The resulting normalized Nusselt correlation is found to be closely approximated by the following seventh-order polynomial.

$$\frac{\mathrm{Nu}}{\mathrm{Nu}_{\max}} = c_0 + c_1\varepsilon_s + c_2\varepsilon_s^2 + c_3\varepsilon_s^3 + c_4\varepsilon_s^4 + c_5\varepsilon_s^5 + c_6\varepsilon_s^6 + c_7\varepsilon_s^7$$

$$\begin{aligned} c_o &= 1.0838\times10^{-3} \quad c_1 = -2.1709\times10^{-2} \\ c_2 &= 2.4268\times10^{0} \quad c_3 = 1.9101\times10^{0} \\ c_4 &= -1.2243\times10^{2} \quad c_5 = 6.1504\times10^{2} \\ c_6 &= -1.1706\times10^{3} \quad c_7 = 7.9093\times10^{2} \end{aligned} \qquad (21)$$

Local heat transfer coefficients were computed using the new model, Eq. 21, a previous Nusselt number correlation for packed beds [11], and an effective solids phase thermal conductivity model [9]. The results are compared to DEM 'ideal' data in Figure 29 (a). In addition, ramp simulations were performed for different parameters and the DEM data was compared to the

new model predictions. Figure 29 (b) shows 200, 300, and 500μm particles flowing down a ramp inclined at an angle of 45°. The particle-particle and particle-wall coefficients of restitution were 0.9, the minimum conduction distance, *s*, was 2.75×10^{-6} cm and the lens radius is 40% larger than the particle radius. The new continuum model is found to be in excellent agreement with heat transfer predicted by DEM, and captures the dependence upon particle size in a quantitative manner.

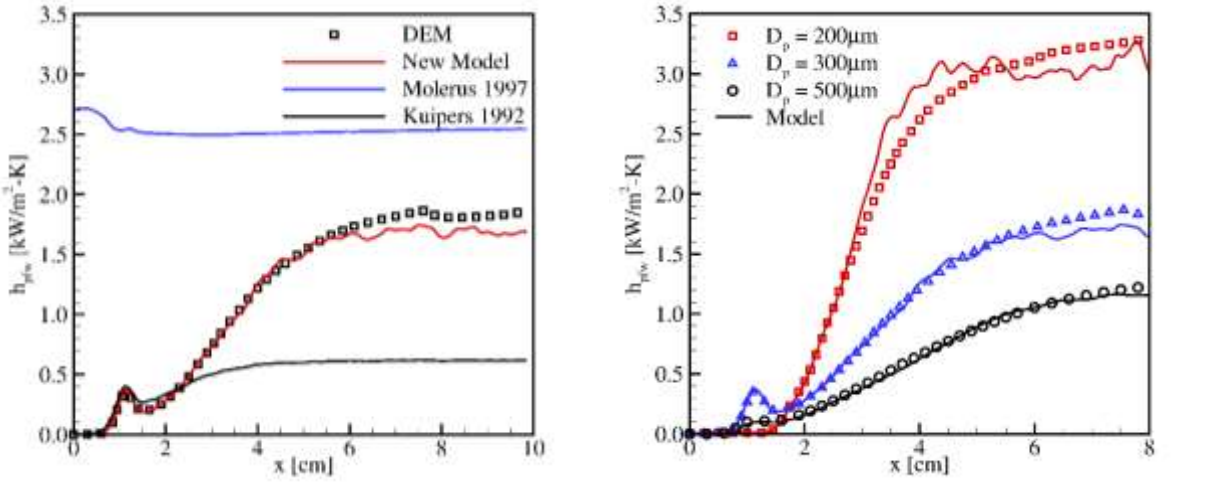

(a) *(b)*

Figure 29. (a) The particle-fluid-wall heat transfer coefficient along the surface of an inclined ramp. The new model and existing models in the literature [9, 11] are compared to DEM data. (b) Comparisons of the new model (lines) to DEM data (symbols) for particle diameters ranging from 200 to 500 μm.

Total Flux Boundary Condition

The resolution of wall temperature gradients within the solar receiver is of great significance, as it is a strong indicator of design feasibility. If thermal gradients within the receiver walls become large, stresses will arise and can lead to mechanical failure. Unfortunately, a thermal boundary condition which accurately describes the receiver system did not exist. Specifically, a constant total heat flux boundary condition with phase heat fluxes that may vary with space and time. Therefore, an extensive amount of effort was devoted to the creation of a new thermal boundary condition which met the aforementioned criteria. To begin with, it was assumed that: (i) all phases experience the same wall temperature, and (ii) the heat transfer to each phase occurs in parallel. Therefore, the total boundary flux may be written as a sum of the heat fluxes to each phase:

$$Q"_w = Q"_g(\mathbf{x}, t) + Q"_s(\mathbf{x}, t) \tag{22}$$

where $Q"_w$ is the total wall heat flux, $Q"_g$ is the heat flux to the gas phase, and $Q"_s$ is the heat flux to the solid phase. By coupling the boundary conditions for the gas phase (continuum) and the solid phase (discrete particles) in this manner, it follows that the phase heat fluxes must be in terms of the same basis. Namely, the heat flux for each particle is resolved by DEM, but the heat flux for numerical cell is resolved by CFD. To give the solids heat flux on a numerical cell basis, the particle heat fluxes within a numerical cell are spatially and temporally averaged:

$$Q"_s(\mathbf{x},t) = \frac{1}{pA_c}\sum_{j=1}^{p}\sum_{i=1}^{n_j} H_{s,i}\left(T_w - T_{p,i}\right) = T_w A - B \tag{23}$$

$$A = \sum_{j=1}^{p}\sum_{i=1}^{n_j}\frac{H_{s,i}}{pA_c} \qquad B = \sum_{j=1}^{p}\sum_{i=1}^{n_j}\frac{H_{s,i}}{pA_c}T_{p,i} \qquad H_{s,i} = h_{pw,i} + h_{pfw,i} \tag{24}$$

where p is the number of DEM time steps per CFD time step, A_c is the area of a CFD numerical cell, n_j is the number of particles doing heat transfer with a wall during the j^{th} DEM time step, $H_{s,i}$ is the total heat transfer coefficient for the i^{th} particle, T_w is the continuum wall temperature, and $T_{p,i}$ is the temperature of particle i. Substitution of the solids heat flux (Eq. 23) and the gas heat flux (Fourier's Law) into Eq. 22 yields a closed form for the total flux into a numerical cell adjacent to a wall. Discretization of said equation yields the following set of relations.

$$Q"_w = \varepsilon_g K_g \frac{\left(T_{g,k} - T_{g,k-1}\right)}{dx_k} + T_{g,k-1/2}A - B \tag{25}$$

$$\frac{\left(T_{g,k} - T_{g,k-1}\right)}{dx_k} + \frac{A}{\varepsilon_g K_g}T_{g,k-1/2} = \frac{Q"_w + B}{\varepsilon_g K_g} \tag{26}$$

$$\frac{\partial T_g}{\partial n} + H_w(\mathbf{x},t)T_g = C(\mathbf{x},t) \tag{27}$$

Inspection of Eq. 26 shows that the proposed description for a total heat flux boundary condition can be formulated into a Robin (or mixed) type boundary condition by setting $H_w = A/\varepsilon_g K_g$ and $C = (Q"_w + B)/\varepsilon_g K_g$. Imposing Eq. 26 on the CFD framework and utilizing the continuum wall temperature for solids conduction (Eq. 1-2) completes the implementation of the new boundary condition. However, to mitigate numerical instabilities the boundary heat flux was linearly ramped from ramped from 0-8500 $[W/m^2K]$ (~ 20% of the design flux) over 1s. By ramping the wall flux, similar to how the CSP will start up, the system is given time to reach hydrodynamic steady state without large step changes in the wall temperatures. I.e., the effective heat transfer coefficient for a cell becomes approximately constant at steady state and thus the wall temperature increases with the wall flux from that point on. The results of simulating Configuration 3 (from Task 5) can be seen below in Figures 30-31. The wall temperatures shown in Figure 30 exhibit the expected qualitative behavior of decreasing with increasing solids concentration, due to high solids heat transfer and the ability of the particles to store significantly more thermal energy than the gas. In addition to qualitative trends, the developed boundary condition is tested in a quantitative manner. Specifically, the average heat flux along the right sidewall of Configuration 3 is tracked throughout the simulation and compared to the imposed boundary flux in Figure 31 (a). The simulated flux is observed to be in excellent agreement with the imposed boundary flux. Furthermore, the phase fluxes are extracted along the same sidewall (at a time of 1.2 s) and illustrated in Figure 31 (b). The total boundary flux is shown to be nearly constant while the phase fluxes vary with space but sum to the boundary flux.

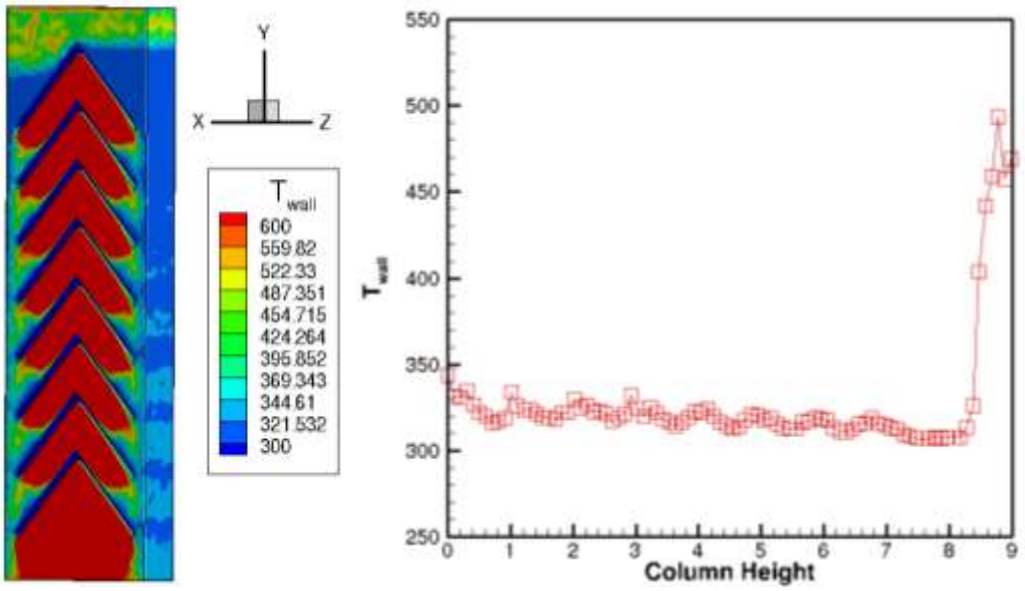

(a) (b)

Figure 30. (a) The predicted wall temperatures [K] for Baffle Configuration 3. (b) The wall temperatures [K] extracted along the column height.

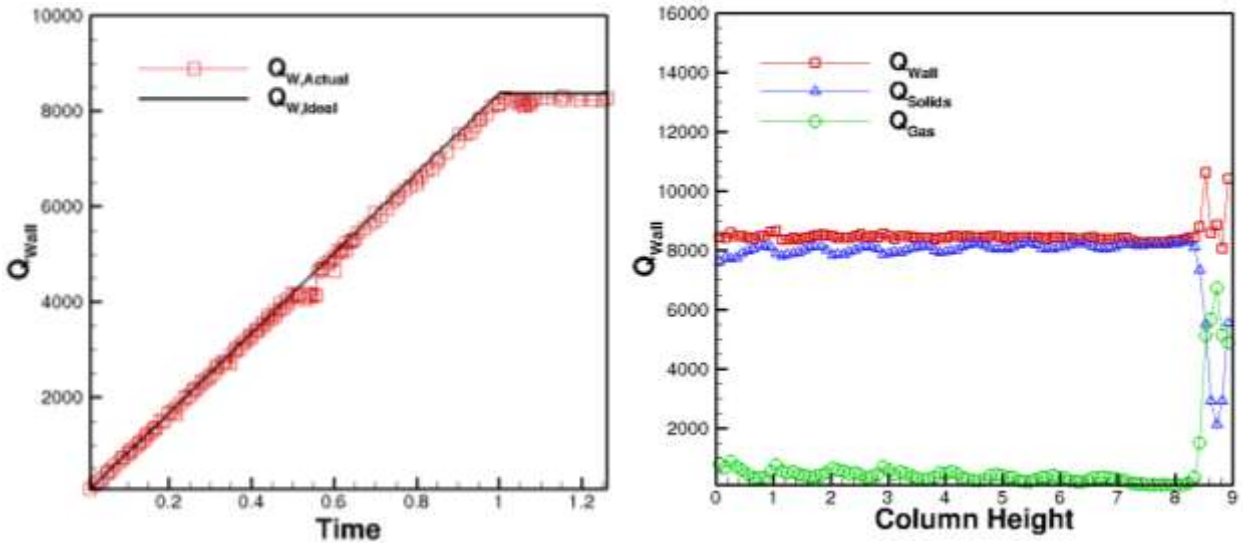

(a) (b)

Figure 31. (a) The actual wall flux [W/m^2s] and ideal flux ramp as a function of simulation time. (b) The total wall flux and fluxes to each phase extracted along the conduit wall at a time of 1.2s show that the phases are indeed coupled.

Inventions, Patents, Publications, and Other Results

List of Publications

Morris, A. B., S. Pannala, Z. Ma, and C. M. Hrenya, "A conductive heat transfer model for particle flows over immersed surfaces, International Journal of Heat and Mass Transfer 89, 1277-1289 (2015).

Morris, A. B., S. Pannala, Z. Ma, and C. M. Hrenya, "Development of soft-sphere contact models for thermal heat conduction in granular flows", Journal of Fluid Mechanics (under review).

Morris, A. B., Z. Ma, S. Pannala, and C. M. Hrenya, "Simulations of heat transfer to solid particles flowing through an array of heated tubes", Solar Energy (under review).

Lattanzi, A. M. and C. M. Hrenya, "A Coupled, Multiphase Constant Heat Flux Boundary Condition for the Discrete Element Method", (under review).

List of Presentations

Apr 2013	Preliminary work was presented by Dr. Zhiwen Ma at the Annual CSP project review meeting (Phoenix, AZ)
Jun 2013	An overview of our BRIDGE objectives as well as our DEM simulation results were presented by Prof. Hrenya at NREL SunShot kickoff meeting (Golden, CO).
Aug 2013	Dr. Morris presented our results at the 2013 NETL Workshop on Multiphase Flows (Morgantown, WV).
Nov 2013:	Conference presentation by Dr. Morris on particle-particle conductive heat transfer at APS DFD 2013 (Pittsburgh, PA).
May 2014	Aaron Morris presented a poster at the Sunshot Summit (Anaheim, CA)
Aug 2014	Benjamin Grote (an undergraduate researcher) presented a poster at the Rocky Mountain Advanced Computing Consortium – won award for best poster
Nov 2014	Christine Hrenya presented AIChE Lectureship Award in Fluidization: "Pachinko Revisited-Predicting granular flows and their heat transfer", 2014 AIChE Annual Meeting (Atlanta, GA)
Jan 2015	Christine Hrenya and Aaron Morris presented "Pachinko Revisited: Predicting gas-solid flows and their heat transfer" - MFS Seminar Series for the DOE National Energy Technology Laboratory.

May 2015	Christine Hrenya was invited to present "Using Computation in Design of Novel Concentrating Solar Power Receiver," - Enabling Processing Innovation through Computation (EPIC) Workshop, Louisiana State University
Jul 2015	Christine Hrenya was invited to present "Development of an improved model for conductive heat transfer to particle flows" - European Solid Mechanics Conference 2015 (Madrid, Spain)
Jul 2015	Christine Hrenya presented "Development of an improved model for conductive heat transfer to particle flows" - Physics Department, University of Extremadura, Badajoz, Spain
Aug 2015	Aaron Morris presented "Simulations of heat transfer to solid particles flowing through an enclosed solar receiver" - 2015 NETL Workshop on Multiphase Flow Science (Morgantown, WV)
Nov 2015	Aaron Morris presents "Discrete Element and Continuum Heat Transfer Simulations of a Solar Receiver That Uses Solid Particles As a Heat Transfer Fluid" – AIChE Annual Meeting (Salt Lake City, UT)

Collaborations Fostered

Dr. Aaron Morris spent several weeks at NETL in Morgantown to work directly with MFIX developers on parallelization and model implementation. Ph.D. candidate Aaron Lattanzi also spent 2 weeks at NETL in Morgantown to work directly with MFIX developers on some outstanding questions and lay the foundation for the total flux boundary condition.

Team members from NREL, ORNL and University of Colorado met monthly via telecom to discuss new results and path forward. This represented a new collaboration between the investigators from different entities.

Path Forward

Follow-on funding was pursued via the SunLamps proposal headed by NREL, though funding was not awarded. A separate proposal was submitted to NSF and awarded for experimental work to validate the DEM and continuum models used here. The NSF effort is fundamental in nature, and thus is less suited to technology transfer and commercialization than was the BRIDGE/SunShot funding.

References

[1] J. Chen, J. Grace, M. Golriz, "Heat transfer in fluidized beds: design methods", *Powder Technology*, **150**, pp 123-132, 2005.

[2] M. Syamlal, W. Rogers, T. O'Brien, "MFIX Documentation Theory Guide", Technical Note, Morgantown Energy Technology Center, Morgantown, WV, 1993.

[3] D. Gidaspow, Multiphase flow and fluidization, Academic Press, San Diego, 1994.

[4] R. Jackson, The dynamics of fluidized particles, Cambridge University Press, New York, 2000

[5] S. Pannala, M. Syamlal, T. O'Brien, eds. Computational gas-solid flows and reacting systems: Theory, methods, and practice. Hershey: IGI Global 2010

[6] J. Musser, Modeling of heat transfer and reactive chemistry for particles in gas-solid flow utilizing continuum-discrete methodology (CDM), PhD Dissertation, West Virginia University, 2011

[7] G. Batchelor and R. O'Brien, "Thermal or electrical conduction through a granular material", *Proc. Of the Royal Society of London. Series A, Mathematic and Physical Sciences*, **355** (1682), pp. 313-333, 1977.

[8] D. Rong and M. Horio, "DEM Simulation of char combustion in a fluidized bed", in *2nd International Conference on CFD in the Minerals and Process Industries*, Melbourne, pp. 65-70, 1999.

[9] Kuipers, W. Prins, W. van Swaaij, "Numerical calculation of wall-to-bed heat-transfer coefficients in gas-fluidized beds", *AIChE Journal*, **38**, pp. 1079-1091, 1992.

[10] C. Wen, T. Chang, "Particle to particle heat transfer in air fluidized beds", *in Proceedings of International Symposium on Fluidization*, 1967.

[11] O. Molerus, "Heat transfer in moving beds with a stagnant interstitial gas", *International Journal of Heat and Mass Transfer*, **40**(17), pp 4151-4159, 1997.

[12] P. Zehner, E. Schlünder, "Wärmeleitfähigkeit von Schüttungen bei mäßigen Temperaturen", *Chemie Ingenieur Technik*, 42(14), pp. 933-941,1970.

[13] Xavier and J. Davidson, "Heat transfer to surfaces immersed in fluidized beds, particularly tube arrays", in *Fluidization: Proceedings of the 2nd Engineering Foundation Conference*, Cambridge, pp. 333-338, 1978.

[14] W.L. Vargas, J. McCarthy, "Conductivity of granular media with stagnant interstitial fluids via thermal particle dynamics simulation", *International Journal of Heat and Mass Transfer*, **45**(24), pp. 4847-4856, 2002.

[15] J.L. Lebowitz, "Exact Solution of Generalized Percus-Yevick Equation for a Mixture of Hard Spheres", *Physical Review*, **133**, A895, 1964.

[16] A. Denloye, J. Botterill, "Heat transfer in flowing packed beds, Chemical Engineering Science," **32**(5), pp 461-465, 1977.

[17] M. Hyde, H. Klocke, "Heat transfer between fluidized beds and heat exchange installations," *International Chemical Engineering*, **20**(4), pp. 583-599,1980.

[18] J. Martinek, Z. Ma, "Granular flow and heat transfer study in a near-blackbody enclosed particle receiver," ASME 8th Intl. Conference on Energy Sustainability, ES2014-6393, 2014.

[19] J. Cai and M. F. Modest, Powder Technology **265** (0), pp. 76-82, 2014.

[20] Morris, A. B., S. Pannala, Z. Ma, and C. M. Hrenya, "A conductive heat transfer model for particle flows over immersed surfaces, International Journal of Heat and Mass Transfer 89, 1277-1289 (2015).

[21] "U.S. Energy Information Administration - EIA - Independent Statistics and Analysis." Annual Energy Review. N.p., n.d. Web. 18 Oct. 2014. <http://www.eia.gov/totalenergy/data/ann.>